EUMETSAT

NWC SAF

SUPPORT TO NOWCASTING AND VERY SHORT RANGE FORECASTING

# Algorithm Theoretical Basis Document for Cloud Physical Properties of the NWC/PPS

NWC/CDOP3/PPS/SMHI/SCI/ATBD/CPP, Issue 2, Rev. 1

*13 December 2018*

## *Applicable to SAFNWC/PPS version 2018*

*Applicable to the following PGEs:*

| Acronym | Product ID | Product name | Version number |
|---|---|---|---|
| CPP | NWC-072 | Cloud Physical Properties | 2.0 |

**Prepared by Swedish Meteorological and Hydrological Institute (SMHI)**

## REPORT SIGNATURE TABLE

| Function | Name | Signature | Date |
|---|---|---|---|
| **Prepared by** | Jan Fokke Meirink (KNMI, CMSAF)<br>Ronald Scheirer (SMHI, NWCSAF)<br>Updates by SMHI | | 13 December 2018 |
| **Reviewed by** | SAFNWC Project Team<br>EUMETSAT | | 3 February 2017 |
| **Authorised by** | Anke Thoss, SMHI<br>*SAFNWC PPS Manager* | | 13 December 2018 |

# DOCUMENT CHANGE RECORD

| Version | Date | Pages | Changes |
|---|---|---|---|
| 1.0d | 22 January 2014 | 37 | Replacing CDOP-document: SAF/NWC/CDOP/SMHI-PPS/SCI/ATBD/5<br>First version for SAFNWC/PPS v2014.<br>Changes:<br>- new document structure<br>- inclusion of scientific updates (summarized in Section 1.6)<br>- added a section describing output, including flags |
| 1.0 | 15 September 2014 | 38 | Response to Actions and RIDs from PCR2014.<br>- Action 4: Provided rationale for using the DAK radiative transfer model in Section 4.2.<br>-Act.7: Both operational and re-processed OSISAF ice maps can be used.<br>- RID LSc-1; formal issues<br>- RID LSc-2: Added a summary of requirements.<br>- RID LSc-6: Replaced term 'cloud type' by 'extended cloud phase' to avoid confusion with the cloud type PGE throughout the document<br>- RID LSc-9: Clarified the use of mid-latitude summer profiles in Section 4.2 and include ozone climatology as input dataset in Section 4.5.2.<br>- RID LSc-12: Clarified in Section 5 that phase is retrieved during day and night<br>- RID PW-37: Clarified correction of ice particle shape in Section 1.6.<br>- RID PW-38: Explained pseudo-spherical correction in Section 4.2<br>- RID PW-39: Elaborated the NIR reflectance and emissivity in Section 4.3.1<br>- RID PW-40: Added introductory sentences in Section 4.3.2<br>- RID PW-41: Clarified cloudy-sky COT in Section 4.4 |
| 2.0d | 23 December 2016 | 40 | First version for SAFNWC/PPS v2018<br>Changes:<br>- Introduced application to MODIS as a proxy for MERSI-2.<br>- Can run on VIIRS data using a mix of I- and M-band channels.<br>- Some additional minor corrections. |
| 2.0 | 20 February 2017 | 39 | Implemented RIDs from PCR-v2018:<br>-Lutz-29: Corrected sub-section numbering in section 4.5.2. |
| 2.1beta | 9 May 2018 | 40 | Document code changed from NWC/CDOP2/PPS/SMHI/SCI/ATBD/5 to NWC/CDOP3/PPS/SMHI/SCI/ATBD/5.<br>Changes for v2018:<br>-Alternative input: CMa-prob. Some alternatives for CTTH-input as well. |
| 2.1d | 17 October 2018 | 39 | Changes for SAFNWC/PPS-v2018 ORR:<br>-Updated scientific references.<br>-Added TBD01, about MERSI-2 usage. |
| 2.1 | 13 December 2018 | 40 | Updates after v2018 ORR:<br>OBJ2_UM_SCI_Heinemann_039: Removed most PGE-<*number*> notations in this document.<br>OBJ2_UM_SCI_Heinemann_041: editorial<br>Other changes:<br>Describe configuration SM_CMAPROB_CLOUD_THRESHOLD. |

# Table of Contents

# List of Tables and Figures

# 1. INTRODUCTION

The EUMETSAT "Satellite Application Facilities" (SAF) are dedicated centres of excellence for processing satellite data, and form an integral part of the distributed EUMETSAT Application Ground Segment ( http://www.eumetsat.int ). This documentation is provided by the SAF on Support to Nowcasting and Very Short Range Forecasting, SAFNWC. The main objective of SAFNWC is to provide, further develop and maintain software packages to be used for Nowcasting applications of operational meteorological satellite data by National Meteorological Services. More information can be found at the SAFNWC webpage, http://nwc-saf.eumetsat.int . This document is applicable to the SAFNWC processing package for polar orbiting meteorological satellites, SAFNWC/PPS, developed and maintained by SMHI ( http://nwcsaf.smhi.se ).

## 1.1. PURPOSE

This document is the Algorithm theoretical Basis Document for the Cloud Physical Properties (CPP) of the SAFNWC/PPS software package.

This document contains a description of the algorithm, including scientific aspects and practical considerations.

## 1.2. SCOPE

This document describes the algorithms implemented in the CPP version 2.0 of the 2018 SAFNWC/PPS software package delivery, with product ID: NWC-072. The official products of SAFNWC/PPS CPP are: LWP and CPH. Additional products are: IWP, COT, REFF and CPH_extended.

It is also worth to notice that the software is developed by, and used in, CM-SAF. CM-SAF used the software (v1.0) for the generation of CLARA-A2 (CLoud Albedo and Radiation dataset using AVHRR, edition 2). In CM-SAF the following product names and product IDs are used for the CLARA-A2 AVHRR products: CPH (CM-11041), LWP (CM-11051) and IWP (CM-11061). COT and REFF are provided as by-products of LWP and IWP.

## 1.3. DEFINITIONS AND ACRONYMS

| Acronym | Explanation |
|---|---|
| **ACPG** | AVHRR/AMSU Cloud Product Generation software (A major part of the SAFNWC/PPS s.w., including the PGEs.) |
| **AEMET** | Agencia Estatal de Meteorología (Spain) |
| **AHAMAP** | AMSU-HIRS-AVHRR Mapping Library (A part of the SAFNWC/PPS s.w.) |
| **AMSU** | Advance Microwave Sounding Unit |
| **AVHRR** | Advanced Very High Resolution Radiometer |
| **CDOP** | Continuous Development and Operational Phase |
| **CDOP-2** | Second Continuous Development and Operational Phase |
| **CM-SAF** | Climate Monitoring SAF |
| **CMA** | Cloud Mask (also PGE01) |
| **CMa-prob** | Cloud Probability (also PGE01c) |
| **CMIC** | Cloud Micro-physics |
| **COT (or $\tau$)** | Cloud Optical Thickness |
| **CPH** | Cloud thermodynamic Phase |
| **CPP** | Cloud Physical Products (also PGE05) |
| **CT** | Cloud Type (also PGE02) |
| **CTTH** | Cloud Top Temperature, Height and Pressure (also PGE03) |
| **CWP** | Cloud Water Path |
| **DAK** | Doubling Adding KNMI |
| **DISORT** | Discrete Ordinate |
| **EPS** | EUMETSAT Polar System |
| **EUMETSAT** | European Organisation for the Exploitation of Meteorological Satellites |
| **IWP** | Ice Water Path |
| **JPSS** | Joint Polar Satellite System (US) |
| **KNMI** | Koninklijk Nederlands Meteorologisch Instituut |
| **LUT** | look-up-table |
| **LWP** | Liquid Water Path |
| **MERSI** | Medium Resolution Spectral Imager |
| **MODIS** | Moderate Resolution Imaging Spectroradiometer |
| **MODTRAN** | MODerate spectral resolution atmospheric TRANsmittance and radiance code |
| **NOAA** | National Oceanic and Atmospheric Administration |
| **NPP** | NPOESS Preparatory Project (relates also to JPSS) |
| **PC** | Precipitating Cloud (also PGE04) |
| **PGE** | Process Generating Element |
| **PPS** | Polar Platform System |
| **REFF (or $r_e$)** | Effective radius |
| **SAF** | Satellite Application Facility |
| **SAFNWC** | Satellite Application Facility for support to NoWcasting |
| **SHDOM** | Spherical Harmonic Discrete Ordinate Method |
| **SMHI** | Swedish Meteorological and Hydrological Institute |
| **SW** | SoftWare |
| **TBC** | To Be Confirmed |
| **TBD** | To Be Defined |
| **TOA** | Top Of Atmosphere |
| **VIIRS** | Visible Infrared Imaging Radiometer Suite |

*Table 1 List of acronyms and abbreviations*

See [RD.1.] for a complete list of acronyms for the SAFNWC project.

## 1.4. REFERENCES

### 1.4.1. Applicable documents

The following documents, of the exact issue shown, form part of this document to the extent specified herein. Applicable documents are those referenced in the Contract or approved by the Approval Authority. They are referenced in this document in the form [AD.X]

For dated references, subsequent amendments to, or revisions of, any of these publications do not apply. For undated references, the current edition of the document referred applies.

Current documentation can be found at SAFNWC Helpdesk web: http://www.nwcsaf.org

| Ref | Title | Code | Vers | Date |
|---|---|---|---|---|
| [AD.1] | NWC SAF Product Requirements Document | NWC/CDOP3/SAF/AEMET/MGT/PRD | 1.1 | 17/12/18 |
| [AD.2.] | NWCSAF Project Plan | NWC/CDOP3/SAF/AEMET/MGT/PP | 1.2 | 10/10/18 |
| [AD.3.] | System and Components Requirements Document for the SAFNWC/PPS | NWC/CDOP3/PPS/SMHI/SW/SCRD | 2.1 | 13/12/18 |

*Table 2: List of Applicable Documents*

### 1.4.2. Reference documents

The reference documents contain useful information related to the subject of the project. These reference documents complement the applicable ones, and can be looked up to enhance the information included in this document if it is desired. They are referenced in this document in the form [RD.X]

For dated references, subsequent amendments to, or revisions of, any of these publications do not apply. For undated references, the current edition of the document referred applies

Current documentation can be found at SAFNWC Helpdesk web: http://www.nwcsaf.org

| Ref | Title | Code | Vers | Date |
|---|---|---|---|---|
| [RD.1.] | The Nowcasting SAF Glossary | NWC/CDOP2/SAF/AEMET/MGT/GLO | 2.1 | 03/02/17 |
| [RD.2] | Validation Report AVHRR GAC cloud products, Edition 1 | SAF/CM/DWD/VAL/GAC/CLD | 2.1 | 27/05/16 |
| [RD.3] | User Manual for the SAFNWC/PPS Application: Science Part | NWC/CDOP3/PPS/SMHI/SCI/UM/INST | 2.0 | 13/12/18 |
| [RD.4] | Scientific and Validation report for the Cloud Product Processors of the NWC/PPS | NWC/CDOP3/PPS/SMHI/SCI/VR/Cloud | 2.0 | 13/12/18 |
| [RD.5] | Algorithm Theoretical Basis Document for the Cloud Mask of the NWC/PPS | NWC/CDOP3/PPS/SMHI/SCI/ATBD/CloudMask | 2.1 | 13/12/18 |
| [RD.6] | Algorithm Theoretical Basis Document for the Cloud Top Temperature, Pressure and Height of the NWC/PPS | NWC/CDOP3/PPS/SMHI/SCI/ATBD/CTTH | 2.1 | 13/12/18 |

*Table 3: List of Referenced Documents*

### 1.4.3. Scientific References

Ackerman, S.A., W.L. Smith, R.E. Revercomb, and J.D. Spinhirne, 1990: The 27–28 October 1986 FIRE IFO Cirrus Case Study: Spectral Properties of Cirrus Clouds in the 8–12 μm Window, *Mon. Wea. Rev.*, **118**, 2377-2388.

Anderson, G. P., S. A. Clough, F. X. Kneizys, J. H. Chetwynd, and E. P Shettle, 1986: AFGL Atmospheric Constituent Profiles (0-120km). Tech. Rep. AFGL-TR-86-0110, 43 pp.

Baum, B. A., P. Yang, A. J. Heymsfield, C. G. Schmitt, Y. Xie, A. Bansemer, Y.-X. Hu, and Z. Zhang, 2011: Improvements in shortwave bulk scattering and absorption models for the remote sensing of ice clouds, *J. Appl. Meteorol. Clim.*, **50**, 1037-1056, doi:10.1175/2010JAMC2608.1.

Berk, A., G. P. Anderson, P. K. Acharya, J. H. Chetwynd, L.S. Bernstein, E. P. Shettle, M. W. Matthew, and S. M. Adler-Golden, 2000: MODTRAN4 Version 2 Users Manual. Technical report, Air Force Materiel Command, Air Force Research Laboratory, Space Vehicles Directorate, Hanscom AFB, MA 01731, USA.

Chandrasekhar S., 1960: *Radiative Transfer*, New York, Dover, 393 pp.

Coakley, J. A., M. A. Friedman, and W. R. Tahnk, 2005: Retrieval of cloud properties for partly cloudy imager pixels, *J. Atmos. Ocean. Technol.*, **22** , 3–17.

Davis, J. M., T. B. McKee, and S. K. Cox, 1985: Application of the Monte Carlo method to problems in visibility using a local estimate: an investigation. *Appl. Optics*, **24**, (19), 3193-3205.

De Haan, J. F., P. Bosma, and J. W. Hovenier, 1987: The adding method for multiple scattering calculations of polarized light, *Astron. Astrophys.*, **183**, 371-391.

Evans, K. F., 1998: The Spherical Harmonics Discrete Ordinate, Method for Three-Dimensional Atmospheric Radiative Transfer. *J. Atmos. Sci.*, **55**, 429-446.

Gao, B.-C. and W. J. Wiscombe, 1994: Surface-induced brightness temperature variations and their effects on detecting thin cirrus clouds using IR emission channels in the 8-12 micron region. *J. Appl. Met.*, **33**, 568-570.

Han, Q., W. B. Rossow, and A. A. Lacis, 1994: Near-Global Survey of Effective Droplet Radii in Liquid Water Clouds Using ISCCP Data. *J. Climate*, **7**, 465-497.

Haywood, J.M., S.R. Osborne, S.J. Abel, 2004: The effect of overlying absorbing aerosol layers on remote sensing retrievals of cloud effective radius and cloud optical depth, *Quart. J. Roy. Meteorol. Soc.*, **130**, 779-800, doi: 10.1256/qj.03.100.

Heidinger, A.K., C. Cao, and J.T. Sullivan, 2002: Using Moderate Resolution Imaging Spectrometer (MODIS) to calibrate advanced very high resolution radiometer reflectance channels, *J. Geophys. Res*., **107**, D23, 4702, doi:10.1029/2001JD002035.

Heidinger, A.K., W.C. Straka III, C.C. Molling, J.T. Sullivan, and X. Wu, 2010: Deriving an inter-sensor consistent calibration for the AVHRR solar reflectance data record, *Int. J. Remote Sensing*, **31**, 6493-6517, doi:10.1080/01431161.2010.496472.

Hess, H, R. B. A. Koelemeijer, and P. Stammes, 1998: Scattering matrices of imperfect hexagonal crystals. *J. Quant. Spectrosc. Radiat. Transfer*, **60**, 301–308.

Jolivet, D., and A. J. Feijt, 2003: Cloud thermodynamic phase and particle size estimation using the 0.67 and 1.6 micron channels from meteorological satellites. *Atm. Chem. Phys. Discuss.*, **3**, 4461-4488.

Karlsson, K.-G., Anttila, K., Trentmann, J., Stengel, M., Meirink, J. F., Devasthale, A., Hanschmann, T., Kothe, S., Jaaskelainen, E., Sedlar, J., Benas, N., van Zadelhoff, G.-J., Schlundt, C., Stein, D., Finkensieper, S., Hakansson, N., and Hollmann, R., 2017: CLARA-A2: the second edition of the CM SAF cloud and radiation data record from 34 years of global AVHRR data, Atmospheric Chemistry and Physics, 17, 5809-5828, doi:10.5194/acp-17-5809-2017.

Knap, W. H., L. C. Labonnote, G. Brogniez, and P. Stammes, 2005: Modeling total and polarized reflectances of ice clouds: evaluation by means of POLDER and ATSR-2 measurements. *Appl. Optics*, **44**, 4060-4073.

Macke, A., D. Mitchell, and L. von Bremen, 1999: Monte Carlo radiative transfer calculations for inhomogeneous mixed phase clouds. *Phys. Chem. Earth*, **24-3**, 237-241.

Marshak, A., S. Platnick, T. Várnai, G. Wen, and R. F. Cahalan, 2006: Impact of three-dimensional radiative effects on satellite retrievals of cloud droplet sizes, *J. Geophys. Res*., **111** , 9207–9218.

McFarquhar, G.M. and A.J. Heymsfield, 1998: The definition and significance of an effective radius for ice clouds, *J. Atmos. Sci*., **55**, 2039-2052.

Meirink, J.F., R.A. Roebeling and P. Stammes, 2009: Atmospheric correction for the KNMI Cloud Physical Properties retrieval algorithm, KNMI publication: TR-304, 17/2/2009, pp22.

Minnis, P., K. N. Liou, and Y. Takano, 1993: Inference of Cirrus Cloud Properties Using Satellite-observed Visible and Infrared Radiances. Part I: Parameterization of Radiance Fields. *J. Atmos. Sci.*, **50**, 1279–1304.

Moody, E. G., M. D. King, S. Platnick, C. B. Schaaf, F. Gao, 2004: Spatially complete global spectral surface albedos: Value-added datasets derived from Terra MODIS land products. *IEEE Trans. Geosci. Remote Sens*., **43**, 144-158.

Moody, E.G., M.D. King, C.B. Schaaf, and S. Platnick, 2008: MODIS-Derived Spatially Complete Surface Albedo Products: Spatial and Temporal Pixel Distribution and Zonal Averages. *J. Appl. Meteorol. Clim*., **47**, 2879–2894.

Nakajima, T., and M. D. King, 1990: Determination of the Optical Thickness and Effective Particle Radius of Clouds from Reflected Solar Radiation Measurements. Part 1: Theory. *J. Atmos. Sci* ., **47**, 1878-1893.

Nakajima, T. Y., and T. Nakajima, 1995: Wide-Area Determination of Cloud Microphysical Properties from NOAA AVHRR Measurements for FIRE and ASTEX regions. *J. Atmos. Sci.*, **52**, 4043 – 4059.

Oreopoulos, L., and R. Davies, 1998: Plane parallel albedo biases from satellite observations. part I: Dependence on resolution and other factors: *J. Climate*, **11** , 919–932.

Pavolonis, M. J. and A. K. Heidinger, 2004: Daytime cloud overlap detection from AVHRR and VIIRS, *J. Appl. Meteorol*., **43**, 762-778.

Pavolonis, M. J., A. K. Heidinger, and T. Uttal, 2005: Daytime global cloud typing from AVHRR and VIIRS: Algorithm description, validation, and comparison, *J. Appl. Meteorol*., **44**, 804-826.

Platnick, S., 2001: A superposition technique for deriving mean photon scattering statistics in plane-parallel cloudy atmospheres, *J. Quant. Spectrosc. Radiat. Transfer*, **68**, 57-73

Platnick, S., King, M. D., Ackerman, S. A., Menzel, W. P., Baum, B. A., Riedi, J. C., Frey, R. A., 2003: The MODIS cloud products: Algorithms and examples from Terra. *IEEE Trans. Geosci. Remote Sens*., **41**, 459-473.

Roebeling, R. A., 2008: Cloud Physical Properties Retrieval for Climate Studies using SEVIRI and AVHRR data, PhD Thesis, Wageningen University, The Netherlands, 160pp. Available from http://www.knmi.nl/publications.

Roebeling, R. A., A. Berk, A. J. Feijt, W. Frerichs, D. Jolivet, A. Macke, and P. Stammes, 2005: Sensitivity of cloud property retrievals to differences in narrow band radiative transfer simulations, KNMI Scientific Report, WR 2005-02, Royal Netherlands Meteorological Institute, De Bilt, the Netherlands, 27 pp. Available from http://www.knmi.nl/publications.

Roebeling, R. A., A. J. Feijt, and P. Stammes, 2006: Cloud property retrievals for climate monitoring: implications of differences between SEVIRI on METEOSAT-8 and AVHRR on NOAA-17, *J. Geophys. Res.*, **111**, D20210, doi:10.1029/2005JD006990.

Rosenfeld, D., E. Cattani, S. Melani, and V. Levizzani, 2004: Considerations on daylight operation of 1.6-versus 3.8-μm channel on NOAA and Metop satellites. *B. Am. Meteorol. Soc.*, **85**, 873–881.

Rossow, W.B., and R.A. Schiffer, 1999: Advances in understanding clouds from ISCCP. *B. Am. Meteorol. Soc*., **80**, 2261-2287.

Seemann, S.W., E. E. Borbas, R. O. Knuteson, G. R. Stephenson, H.-L. Huang, 2008: Development of a Global Infrared Land Surface Emissivity Database for Application to Clear Sky Sounding Retrievals from Multi-spectral Satellite Radiance Measurements, *J. Appl. Meteorol. Clim.*, **47**, 108-123.

Seethala, C., 2011: Evaluating the diurnal cycle of clouds using CM-SAF SEVIRI VIS/NIR and TMI microwave retrievals, CM-SAF VS/AS19 report, 69pp. Available from http://www.cmsaf.eu.

Seethala, C. and A. Horvath, 2010: Global assessment of AMSR-E and MODIS cloud liquid water path retrievals in warm oceanic clouds, *J. Geophys. Res*., **115**, D13202, doi:10.1029/2009JD012662.

Segelstein, D., 1981: The complex refractive index of water, M.Sc. Thesis, Univ. of Missouri, Kansas City.

Schumann, U., B. Mayer, K. Gierens, S. Unterstrasser, P. Jessberger, A. Petzold, C. Voigt, J.-F. Gayet, 2011: Effective radius of ice particles in cirrus and contrails. *J. Atmos. Sci.*, **68**, 300–321, doi:10.1175/2010JAS3562.1.

Stammes, P., 2001: Spectral radiance modeling in the UV-Visible range. IRS 2000: Current problems in Atmospheric Radiation, edited by W.L. Smith and Y.M. Timofeyev, pp 385-388, A. Deepak Publ., Hampton, Va.

Stamnes, K., S. C Tsay, W. Wiscombe, and K Jayaweera, 1988: Numerically stable algorithm for discrete ordinate method radiative transfer in multiple scattering and emitting layered media. *Appl. Optics*, **27**, 2502-2509.

Stephens, G. L., 1978: Radiation profiles in extended water clouds: II. Parameterization schemes. *J. Atmos. Sci.*, **35**, 2123-2132.

Stephens, G. L. and C. D. Kummerow, 2007: The Remote Sensing of Clouds and Precipitation from Space: A Review. *J. Atmos. Sci*., **64** , 3742–3765.

Van der A, R. J., Allaart, M. A. F., and Eskes, H. J., 2010: Multi sensor reanalysis of total ozone, Atmos. Chem. Phys., 10, 11277–11294, doi:10.5194/acp-10-11277-2010.

Warren, S. G. and R. E. Brandt, 2008: Optical constants of ice from the ultraviolet to the microwave: A revised compilation. *J. Geophys. Res.*, **113**, D14220, doi:10.1029/2007JD009744.

Watts, P. D., C. T. Mutlow, A. J. Baran, and A. M. Zavody, 1998: Study on Cloud Properties derived from Meteosat Second Generation Observations, Final Report, EUMETSAT ITT no. 97/181.

Wilcox, E. M., Harshvardhan, and S. Platnick, 2009: Estimate of the impact of absorbing aerosol over cloud on the MODIS retrievals of cloud optical thickness and effective radius using two independent retrievals of liquid water path, *J. Geophys. Res*., **114**, D05210, doi:10.1029/2008JD010589.

Wolters, E. L .A., H. M. Deneke, B. J. J. M. van den Hurk, J. F. Meirink, and R. A. Roebeling, 2010: Broken and inhomogeneous cloud impact on satellite cloud particle effective radius and cloud-phase retrievals, *J. Geophys. Res*., **115**, doi:10.1029/2009JD012205.

Wolters, E. L. A., R. A. Roebeling, and P. Stammes, 2006: Cloud reflectance calculations using DAK: study on required integration points, KNMI Technical Report, TR-292, Royal Netherlands Meteorological Institute, De Bilt, The Netherlands, 17 pp. Available from http://www.knmi.nl/publications.

Yang, P., L. Bi, B. A. Baum, K.-N. Liou, G. W. Kattawar, M. I. Mishchenko, and B. Cole, 2013: Spectrally consistent scattering, absorption, and polarization properties of atmospheric ice crystals at wavelengths from 0.2 to 100 μm, *J. Atmos. Sci*., **70**, 330-347, doi:10.1175/JAS-D-12-039.1.

Zhang, Z., A. S. Ackerman, G. Feingold, S. Platnick, R. Pincus, and H. Xue, 2012: Effects of cloud horizontal inhomogeneity and drizzle on remote sensing of cloud droplet effective radius: Case studies based on large-eddy simulations, *J. Geophys. Res.*, **117**, D19208, doi:10.1029/2012JD017655.

Zhang, Z., and S. Platnick, 2011: An assessment of differences between cloud effective particle radius retrievals for marine water clouds from three MODIS spectral bands, *J. Geophys. Res*., **116**, D20215, doi:10.1029/2011JD016216.

Zhang, Z., P. Yang, G. Kattawar, Riedi, J., Labonnote, L. C., Baum, B. A., Platnick, S., and Huang, H.-L., 2009: Influence of ice particle model on satellite ice cloud retrieval: lessons learned from MODIS and POLDER cloud product comparison, *Atmos. Chem. Phys*., **9**, 7115-7129, doi: 10.5194/acp-9-7115-2009.

Zinner, T., G. Wind, S. Platnick, and A.S. Ackerman, 2010: Testing remote sensing on artificial observations: impact of drizzle and 3-D cloud structure on effective radius retrievals, *Atmos. Chem. Phys*., **10**, 9535-9549, doi:10.5194/acp-10-9535-2010.

## 1.5. DOCUMENT OVERVIEW

The set-up of this document is as follows. In Section 3 a short overview of the retrieval algorithms is presented. Section 4 gives a detailed description of the retrieval algorithms, consisting of the relevant underlying physics (Section 4.1), the radiative transfer modelling (Section 4.2), the implementation of the retrieval scheme (Section 4.3), the error budget of the retrieved products (Section 4.4), and the practical application of the algorithms (Section 4.5). Finally, assumptions and limitations are discussed in Section 5.

## 1.6. SCIENTIFIC UPDATES SINCE PPS VERSION 2014

The only update compared to PPS Version 2014 is that the CPP software has been adapted to MODIS, serving as a proxy for future MERSI-2 operation.

There is a new PPS product, Cloud Probability. As input to CPP can be used Cloud Mask (as before) or Cloud Probability (configurable).

# 2. INTRODUCTION TO THE SAFNWC/PPS CLOUD PHYSICAL PROPERTIES PRODUCT

This SAFNWC Algorithm Theoretical Basis Document (ATBD) provides detailed information on the retrieval algorithm deriving cloud physical properties (CPP) products from VIS-NIR-IR satellite imagers. The algorithm retrieves cloud-top phase and liquid water path as official products. Cloud optical thickness, effective radius, ice water path, and an extended cloud-top phase are derived as additional products.

*Table 4: Overview of SAF products covered in this ATBD.*

| Cloud property | Explanation | Status in NWCSAF/PPS |
|---|---|---|
| CPH | Cloud-top thermodynamic phase | Official product |
| LWP | cloud liquid water path | Official product |
| CPH_extended | Cloud-top thermodynamic phase, more classes than in CPH | Additional product |
| IWP | Cloud ice water path | Additional product |
| COT | cloud optical thickness | Additional product |
| REFF | Cloud particle effective radius | Additional product |

Further details about these cloud physical property software can be found in the product user manual ([RD.3]). The requirements for the SAFNWC/PPS CPP products can be found in [AD.1]. The quality of the official products, CPH and LWP, is discussed in the validation report [RD.4].

The software is used by CM-SAF to generate climate data records of cloud properties. Their AVHRR-based climate record named CLARA-A2 (Karlsson et al., 2017), including the cloud physical properties, was extensively validated in [RD.2]. The algorithm description in this ATBD is originally based on Roebeling (2008) and Roebeling et al. (2006), but contains a range of modifications and improvements implemented since then.

The cloud physical properties retrieval algorithm requires a cloud mask and cloud-top height and temperature as input. The SAFNWC/PPS algorithms for these products are described in [RD.5] and [RD.6].

## 2.1. REQUIREMENTS

The requirements for the SAFNWC/PPS products are described in the Product Requirements Document [AD.1]. In Table 5 and Table 6 is given a summary of the requirement specific for the cloud physical properties product.

*Table 5 Accuracy requirements for CPP Cloud Phase*

| | Water POD | Water FAR | Ice POD | Ice FAR |
|---|---|---|---|---|
| **Threshold accuracy** | 70% | 35% | 60% | 35% |

| | | | | |
|---|---|---|---|---|
| **Target accuracy** | 80% | 20% | 80% | 20% |
| **Optimal accuracy** | 90% | 10% | 90% | 10% |

*Table 6 Accuracy requirements for CPP Liquid Water Path*

| | **RMS** | **Bias** |
|---|---|---|
| **Threshold accuracy** | 100 $g/m^2$ | 20 $g/m^2$ |
| **Target accuracy** | 50 $g/m^2$ | 10 $g/m^2$ |
| **Optimal accuracy** | 20 $g/m^2$ | 5 $g/m^2$ |

# 3. ALGORITHM OVERVIEW

The CPP (cloud physical properties) algorithm consists of two main parts. First, the cloud-top thermodynamic phase (CPH) is determined from a cloud typing approach following Pavolonis and Heidinger (2004) and Pavolonis et al. (2005). This cloud phase algorithm consists of a series of spectral tests applied to infrared brightness temperatures. It has a nighttime branch as well as a daytime branch in which shortwave reflectances are considered in addition.

The algorithm then proceeds with retrieving cloud optical thickness (COT or $\tau$) and cloud particle effective radius (REFF or $r_e$), as well as liquid/ice water path (LWP/IWP), during daytime given the thermodynamic phase determined before. This retrieval scheme was developed at KNMI, first described in Roebeling et al. (2006), and is based on earlier methods that retrieve cloud optical thickness and cloud particle effective radius from satellite radiances at wavelengths in the non-absorbing visible and the moderately absorbing solar infrared part of the spectrum (Nakajima and King 1990; Han et al. 1994; Nakajima and Nakajima 1995; Watts et al. 1998).

# 4. ALGORITHM DESCRIPTION

## 4.1. THEORETICAL DESCRIPTION

The principle of the CPP retrieval algorithm is that the reflectance of clouds at a non-absorbing wavelength in the visible region (VIS: 0.6 or 0.8 μm) is strongly related to the optical thickness and has little dependence on particle size, whereas the reflectance of clouds at an absorbing wavelength in the near-infrared region (NIR: 1.6 or 3.8 μm) is primarily related to particle effective radius. This feature allows the retrieval of COT and REFF from two channels of a passive imager. Moreover, Figure 1 shows that the imaginary parts of the refractive indices of water and ice, which are a measure for absorption, differ. For example, around 1.6 and 3.8 μm ice particles are more absorbing than water droplets. This feature, together with a series of spectral tests on the thermal infrared (IR) window channels is used to retrieve cloud-top thermodynamic phase.

The cloud optical thickness is defined at 0.6 μm under the assumption of a plane parallel atmosphere with reference to a vertical transect. The particle effective radius $r_e$ is the relevant quantity for radiative scattering, and is given by the ratio of the mean particle volume to the mean projected cross-sectional area A (e.g., Schumann et al., 2011):

$$r_e = (3V)/(4A) \qquad (1)$$

In case of a collection of spherical water droplets, this can be rewritten to:

$$r_e = \frac{\int_0^\infty r^3 n(r) dr}{\int_0^\infty r^2 n(r) dr}, \qquad (2)$$

where $r$ is the droplet radius, and $n(r)\,dr$ is the number of particles per unit volume with radius between $r$ and $r+dr$.

Liquid Water Path (LWP) is computed from the retrieved $\tau$ and $r_e$ by (Stephens 1978):

$$LWP = \frac{2}{3}\tau r_e \rho_l \,, \qquad (3)$$

where $\rho_l$ = 1 g cm$^{-3}$ is the density of water. Ice Water Path (IWP) is computed analogously, but using the density of ice, $\rho_i$ = 0.93 g cm$^{-3}$.

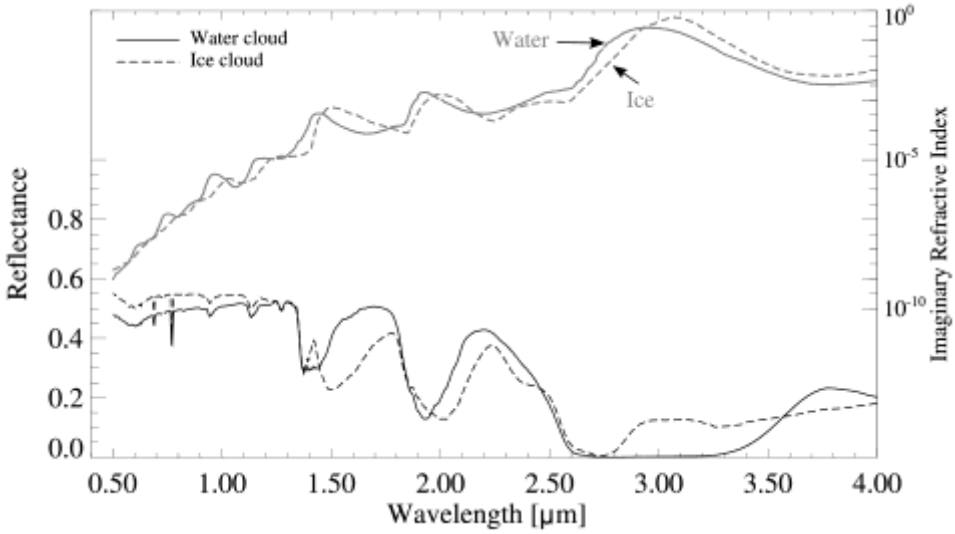


*Figure 1 Simulated top-of-atmosphere (TOA) reflectance spectra for a stratocumulus (water) cloud and a cirrus (ice) cloud, and the imaginary part of the index of refraction of water and ice. The simulations were made with MODTRAN at $\theta_0$ = 45°, $\theta$ = 0° and $\varphi$ = 0°. The reflectances are plotted as black lines, while the refractive indices are plotted as gray lines*

## 4.2. RADIATIVE TRANSFER

The CPP algorithm compares satellite observed reflectances at visible and near-infrared wavelengths to look-up tables (LUTs) of simulated reflectances for given cloud optical thicknesses, particle sizes and surface albedos for water and ice clouds (Watts et al. 1998; Jolivet and Feijt 2003). The Doubling Adding KNMI (DAK) radiative transfer model (RTM) has been used to generate the LUTs of simulated cloud reflectances. DAK has been developed for line-by-line or monochromatic multiple scattering calculations at UV, visible and near infrared wavelengths in a horizontally homogeneous cloudy atmosphere using the doubling-adding method (De Haan et al. 1987; Stammes 2001). A pseudo-spherical correction is used as in Caudill et al. (1997). This correction accounts for attenuation of the solar beam as in a spherical atmosphere, while higher-order scattering is calculated for a plane-parallel atmosphere. DAK has been selected because it is the KNMI in-house shortwave RTM, and there is ample hands-on experience with this RTM at KNMI. Furthermore, comparisons with other RTMs have been performed, showing generally favourable results for DAK (see also Section 4.4).

Clouds are assumed to be plane-parallel and embedded in a multi-layered Rayleigh scattering atmosphere. The particles of water clouds are assumed to be spherical droplets with effective radii between 3 and 34 μm and an effective variance of 0.15. For ice clouds, imperfect (or roughened), randomly oriented, hexagonal ice crystals in monodisperse size distributions with effective radii between 5 and 80 μm are assumed. Scattering properties were calculated with Mie theory for spherical droplets and with a raytracing code using the geometric optics approximation

(Hess et al. 1998) for the hexagonal ice crystals. Knap et al. (2005) demonstrated that roughened hexagonal crystals give adequate simulations of total and polarized reflectances of ice clouds.

Scattering phase functions of water droplets and ice crystals are compared in Figure 2. For water droplets a strong reduction in sideways scattering is observed as well as enhanced scattering at the rainbow angle and in backscatter direction. Smooth ice crystals tend to yield distinct halo features and a strong backscatter peak. In contrast, roughened crystals show virtually featureless phase functions, and also yield considerably lower asymmetry parameters compared to smooth crystals (Zhang et al., 2009). The recently revised phase functions for the official MODIS retrievals, based on a size distribution of a collection of roughened ice crystal shapes (Baum et al., 2011), are also plotted in Figure 2. They are remarkably similar to our phase functions, demonstrating that roughening has a far larger impact on phase functions than particle shape and size distribution.

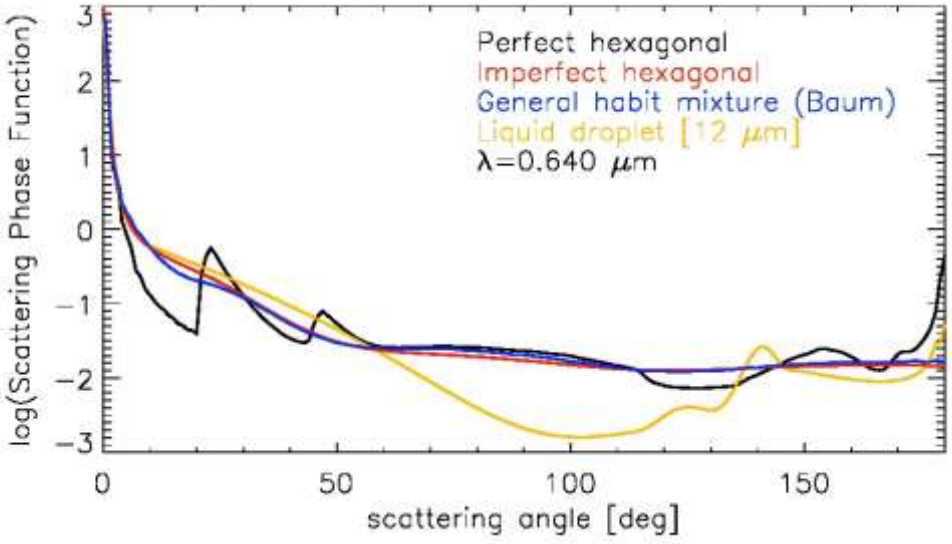


*Figure 2 Comparison of scattering phase functions of water droplets, perfect (smooth) hexagonal ice crystals, imperfect (roughened) hexagonal ice crystals, and the Baum et al. (2011) roughened ice crystal habit mixture. The wavelength is 0.64 μm and the effective radii are 12 μm for the water droplets and 10 μm for the ice crystals.*

Figure 3 shows an example of DAK calculations of 0.6 and 1.6/3.8 μm reflectances as function of τ and $r_e$ for water droplets and ice crystals. The figure illustrates that for optically thick clouds lines of equal τ and particle size are nearly orthogonal, meaning that the 0.6 and 1.6/3.8 μm reflectances contain independent information on τ and $r_e$, respectively. This is not the case for optically thin clouds. Moreover, for these clouds, the lines of different $r_e$ are very close together, implying that the retrieval of particle size is inherently uncertain. Further, it is evident that ice clouds have lower 1.6-μm and 3.8-μm reflectances than water clouds, which is a consequence of the stronger absorption of ice particles compared to water droplets at these wavelengths (see Figure 1). Although the features of the absorbing channels at 1.6 and 3.8 μm are similar, there are clear differences. At 3.8 μm the absorption by both water and ice is much stronger than at 1.6 μm. As a result, the dynamical range of reflectance is lower, but lines of equal τ and $r_e$ are more orthogonal.

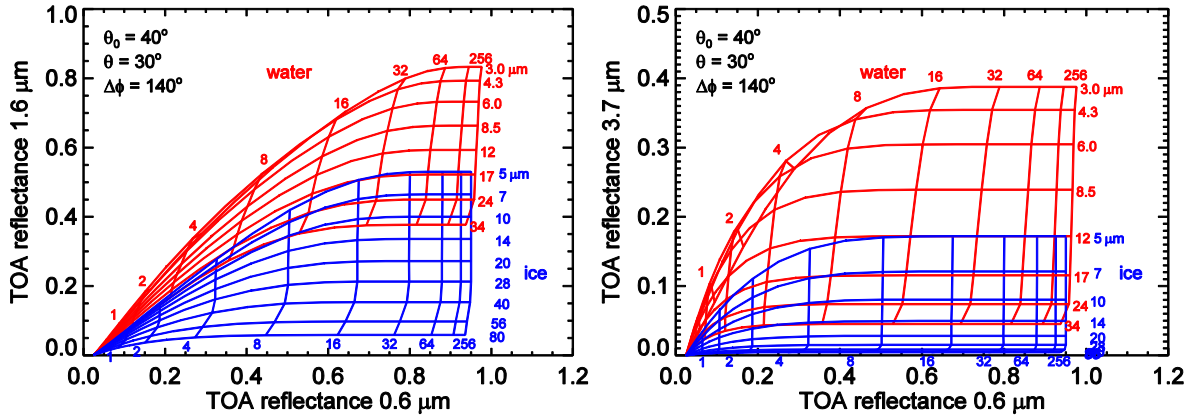


*Figure 3 DAK calculations of TOA reflectance at 0.6 µm versus (a) 1.6 µm and (b) 3.8 µm for clouds consisting of spherical water droplets (red curves) and imperfect hexagonal ice columns (blue curves). The reflectances have been calculated over a black surface (albedo = 0). Solar and satellite angles are indicated in the plots. The vertically oriented lines represent lines of equal cloud optical thickness, while the horizontally oriented lines represent lines of equal particle size. Values of optical thickness and effective radius are indicated in the plot. Note the different scaling of the vertical axis in panels (a) and (b).*

*Table 7 Properties of the cloudy atmosphere that are used for the radiative transfer calculations to generate the LUTs.*

| ***Parameter*** | ***Settings*** | |
|---|---|---|
| Vertical profiles of pressure, temperature, and ozone | Midlatitude summer [a)] | |
| Aerosol model | None | |
| Cloud height | Water clouds: 1000-2000 m; Ice clouds: 5000-6000 m | |
| Solar zenith angle ($\theta_0$) [b)] | 0 - 84.3° (73 Gaussian points in $\mu_0 = \cos(\theta_0)$) | |
| Viewing zenith angle ($\theta$) [b)] | Same as $\theta_0$ | |
| Relative azimuth angle ($\phi$) [b)] | 0 - 180° (equidistant, 91 points) | |
| Cloud optical thickness | 0 – 256 (equidistant in log(τ), 22 points) | |
| | **water clouds** | **ice clouds** |
| Cloud particle type | Spherical water droplet | Imperfect hexagonal ice crystal [c)] |
| Cloud particle size | 3–34 µm<br>equidistant in log($r_e$), 8 points | 5–80 µm<br>equidistant in log($r_e$), 9 points |
| Liquid / Ice water path | 0 – 5,800 g m$^{-2}$ | 0 – 12,700 g m$^{-2}$ |
| Size distribution | Two-parameter gamma | - |
| Effective variance ($v_e$) | 0.15 [d)] | - |
| Complex refractive index | Segelstein (1981) | Warren and Brandt (2008) |

[a)] The midlatitude summer (MLS) atmosphere model was taken from Anderson et al. (1986). The choice of the temperature and pressure profile has a marginal impact on the LUT, namely only through Rayleigh scattering. Deviations from the MLS total column ozone are taken into account in the atmospheric correction procedure, see Eq. (5).

[b)] The chosen distributions of angles are motivated in Wolters et al. (2006).

[c)] Aspect ratios of the imperfect hexagonal crystals are taken from Table 1 in Yang et al. (2013). To simulate the roughening a distortion angle of 30° is applied.

[(d)] This value is within the range found from in situ measurements. Different choices are possible, but the impact on the retrieved cloud properties is modest.

Table 7 summarizes the governing characteristics of the cloudy atmosphere, together with information about intervals of cloud properties and viewing geometries used in the DAK simulations to generate the LUT. The DAK simulations were done for a black surface. The TOA reflectance $R(\alpha_s)$ over a surface with reflectance $\alpha_s$ is computed using (Chandrasekhar, 1960):

$$R(\alpha_S) = R(\alpha_S = 0) + \frac{\alpha_s t_c(\theta_0) t_c(\theta)}{1 - \alpha_s \alpha_a} \qquad (4)$$

Here, $t_c(\theta_0)$ and $t_c$ $(\theta)$ are the cloud transmissivities at the solar and viewing zenith angles, respectively, and $\alpha_a$ is the hemispherical sky albedo for upwelling, isotropic radiation. The required parameters are determined from two additional DAK calculations with surface reflectance values of 0.5 and 1.0.

The DAK calculations concern monochromatic radiative transfer at a wavelength close to the centre of the respective satellite imager narrowbands. These calculations neglect scattering and absorption by atmospheric gases, except for Rayleigh scattering by air molecules and absorption by ozone. Before the reflectance simulated by DAK can be compared to an observed reflectance, the absorption by atmospheric gases in the band has to be taken into account. This so-called atmospheric correction has been implemented based on MODTRAN4.2 (Berk et al. 2000) radiative transfer simulations. The atmosphere-corrected TOA reflectance ($R_{atm.corr.}$) is calculated as:

$$R_{atm.corr.} = R\, t_{a,ac}(\theta_0, H_c, WVP, TCO) t_{a,ac}(\theta, H_c, WVP, TCO), \qquad (5)$$

where $t_{a,ac}$ is the above-cloud atmospheric transmissivity simulated by MODTRAN using a Lambertian surface placed at the cloud top height ($H_c$) and for a given water vapor path (WVP) and total column ozone (TCO). The two-way transmissivity, i.e. the product of the two transmissivities in Eq. (5), is a function of the geometrical air mass factor (AMF = $1/\mu_0 + 1/\mu$). This two-way transmissivity is stored in a LUT with dimensions AMF, $H_c$, WVP, and TCO. Absorption by trace gases within and below the cloud is neglected. An indication of the magnitude of the atmospheric correction is given in Table 8. Note that the atmospheric correction depends on the exact spectral response of the specific instrument channels.

*Table 8 Typical magnitude of atmospheric correction, expressed as 1 minus the two-way transmissivity, in %. The numbers have been calculated for a reference atmosphere ($H_c$ = 2 km, AMF = 2, TCO = 332 DU, and WVP = 30 kg m$^{-2}$), based on the NOAA-15 AVHRR spectral response, and for individual absorbing gases as well as for all gases together.*

| Gas | Channel 1 | Channel 3a | Channel 3b |
|---|---|---|---|
| $H_2O$ | 0.6 % | 0.2 % | 11.9 % |
| $O_3$ | 0.7 % | - | - |
| $O_2$ | 0.1 % | - | - |
| $CO_2$ | | 3.1 % | 0.2 % |
| $CH_4$ | | 0.1 % | 3.7 % |
| $N_2O$ | | | 1.6 % |
| $N_2$-continuum | | | 0.7 % |
| All gases | 1.5 % | 3.4 % | 17.6 % |

More details on the implementation of atmospheric correction and the effect on retrieved cloud properties can be found in Meirink et al. (2009).

Whereas at 1.6 μm reflected sunlight is the only significant component of the measured TOA radiance, at 3.8 μm thermal emission by the surface, atmosphere and clouds provides a non-negligible contribution. Thermal emission is expressed as a reflectance ($R_e$), and calculated as the sum of contributions from surface ($R_{e,s}$) and cloud ($R_{e,c}$) following Nakajima and Nakajima (1995):

$$R_e = R_{e,s} + R_{e,c} = \left(\varepsilon_s B_\lambda(T_s) t_a(\theta) t_c(\theta) + \varepsilon_c B_\lambda(T_c) t_{a,ac}(\theta)\right) \frac{\pi}{\mu_0 F_{0,\lambda}}., \qquad (6)$$

where $\varepsilon_s$ is the surface emissivity, $T_s$ and $T_c$ are the surface and cloud-top temperatures, respectively, $B_\lambda(T)$ is the Planck function at temperature $T$ and wavelength $\lambda$ (= 3.8 μm), $F_{0,\lambda}$ is the extraterrestrial solar flux at wavelength $\lambda$, and $\varepsilon_c$ is the cloud emissivity approximated as:

$$\varepsilon_c = 1 - t_c(\theta_0) - R(\theta_0, \theta, \phi). \qquad (7)$$

$\varepsilon_c$ is a function of $\tau$ and $r_e$ through the cloud transmissivity $t_c$ and reflectivity $R$. The retrieval procedure is the same as for the 1.6-μm channel with the observed 3.8-μm radiance converted to a reflectance which is compared with the sum of simulated reflected sunlight and thermal emission.

## 4.3. RETRIEVAL SCHEME

The CPP retrieval scheme consists of two parts. The first part is the retrieval of an extended cloud phase, and is described in Section 4.3.1. This extended phase is then reduced to two categories: liquid and ice. The second part is the retrieval of cloud optical properties (optical thickness and effective radius) for the retrieved phase. This is further described in Section 4.3.2.

### 4.3.1. Cloud phase

The cloud phase retrieval is based on a number of threshold tests using AVHRR channels 3a, 3b, 4 and 5 or corresponding channels from VIIRS, MODIS or MERSI-2 (see Section 4.5.1). The algorithm is run for cloudy pixels and yields one of the following extended cloud phase categories: fog, liquid, supercooled, opaque ice, cirrus, and overlap. Separate retrieval schemes are applied during daytime and nighttime. An extensive motivation for and description of the several spectral tests is given in Pavolonis and Heidinger (2004) and Pavolonis et al. (2005). Here, we provide a complete overview of the spectral tests and the order in which they are performed. Values of the thresholds are given in ANNEX B.

The algorithm contains a number of tests using the 3.8 μm reflectance ($R_{3.8}$) during daytime or emissivity ($\varepsilon_{3.8}$) during night time. These are estimated from the 3.8 and 11 μm radiances alone. For the 3.8 μm radiance $L_{3.8}$ we have:

$$L_{3.8} = R_{3.8} \frac{\mu_0 F_{0,3.8}}{\pi} + \varepsilon_{3.8} L_{bb,3.8}, \qquad (8)$$

where $L_{bb,3.8}$ is the black-body radiance at 3.8 μm. Assuming an 11 μm emissivity of one (i.e. opaque clouds) yields:

$$L_{bb,3.8} = B_{3.8}(T_{bb}) = B_{3.8}(T_{11}) \qquad (9)$$

where $T_{11}$ is the brightness temperature at 11 μm and $T_{bb}$ is the blackbody temperature. Assuming then also zero 3.8 μm transmissivity (again: opaque clouds), we have:

$$\varepsilon_{3.8} = 1 - R_{3.8}. \qquad (10)$$

Inserting Eqs. (9) and (10) in (8) yields:

$$R_{3.8} = \frac{L_{3.8} - B_{3.8}(T_{11})}{\mu_0 F_{0,3.8}/\pi - B_{3.8}(T_{11})}, \qquad (11)$$

and the emissivity during night time is:

$$\varepsilon_{3.8} = L_{3.8} / B_{3.8}(T_{11}). \qquad (12)$$

.

As stated above, these relations assume opaque clouds. Indeed, the NIR reflectance tests are less reliable for thin clouds (see Pavolonis et al. 2005, Sect. 6).The algorithm starts with an initial cloud phase assignment based on $T_{11}$:

- $T_{11} \leq 253.16$ K → opaque ice
- 253.16 K < $T_{11} \leq 273.16$ K → supercooled
- $T_{11} > 273.16$ K → water

The *daytime* ($\theta_0 < 88^o$) algorithm then proceeds with the following tests, in which $R_{NIR}$ is either $R_{1.6}$ or $R_{3.8}$, depending on the available channel.

d1: First NIR reflectance test

Clouds classified as supercooled, with $T_{11} < 263.16$ K, and $R_{NIR} \leq$ NIR_PHASE_THRES, are re-set to opaque_ice. Here, NIR_PHASE_THRES depends on the NIR channel used and the surface type (see Appendix).

d2: Second NIR reflectance test ('inverse' of d1)

Clouds classified as opaque ice, with $T_{11} > 233.16$ K, and $R_{NIR} >$ NIR_PHASE_THRES, are re-set to supercooled.

d3: Cloud overlap test

Clouds with a $T_{11}$ - $T_{12}$ difference larger than BTD1112_DOVERLAP_THRES, with 210 K < $T_{11} < 270$ K, with $R_{NIR} >$ NIR_OVER_THRES, and not over desert, are set to overlap. Here, BTD1112_DOVERLAP_THRES depends on $R_{0.6}$, as well as on $\theta$ and $\theta_0$, and NIR_OVER_THRES depends on the NIR channel used and the surface type (see Appendix).

d4: Cirrus test

Clouds with a $T_{11}$ - $T_{12}$ difference larger than BTD1112_CIRRUS_THRES, with $T_{11} < 295$ K, with $R_{NIR} <$ NIR_CIRRUS_THRES, and not classified as overlap, are set to cirrus. The $R_{NIR}$ criterion is not applied if $\theta_0 > 70^o$, but the cirrus is assigned a 'low quality' in this case. BTD1112_CIRRUS_THRES depends on $T_{11}$ and $\theta$, and NIR_CIRRUS_THRES depends on the NIR channel used and the surface type (see Appendix).

d5: Fog test

Only performed if ch3b is available: if $R_{3.8} \geq 0.25$, $R_{3.8}/R_{0.6} < 0.6$, $T_{11} > 240$ K, and the surface is not desert, the cloud is classified as fog.

The *nighttime* ($\theta_0 \geq 88^o$) algorithm proceeds with the following tests.

n1: First 3.8 μm emissivity test

Clouds classified as supercooled, with $T_{11} < 263.16$ K, and $\varepsilon_{3.8} \geq$ EMS38_PHASE_THRES, are re-set to opaque_ice. Here, EMS38_PHASE_THRES depends on $T_{11}$.

n2: Second 3.8 μm emissivity test ('inverse' of n1)

Clouds classified as opaque ice, with $T_{11} > 233.16$ K, and $\varepsilon_{3.8} <$ EMS38_PHASE_THRES, are re-set to supercooled.

n3: Cloud overlap test

Clouds with BTD1112_NOVERLAP_THRES_L < $T_{11}$ - $T_{12}$ < BTD1112_NOVERLAP_THRES_H, 210 K < $T_{11}$ < 283 K, and EMS38_NOVERLAP_THRES_L < $\varepsilon_{3.8}$ < EMS38_NOVERLAP_THRES_H are set to overlap. Here, the thresholds vary between tropical and extratropical areas, and between surface types (see Appendix).

n4a: First cirrus test

Clouds with $T_{11}$ - $T_{12}$ > BTD1112_CIRRUS_THRES and $\varepsilon_{3.8} > 1.3$, and not classified as overlap, are set to cirrus.

n4b: Second cirrus test

Clouds with $T_{11} < 300$ K and $\varepsilon_{3.8} > 1.1$, and not classifed as overlap or opaque ice, are set to cirrus.

n5: Fog test

If $\varepsilon_{3.8} \leq 0.9$, $T_{11} > 240$ K, $\theta_0 \geq 90^o$ and the surface is not desert, the cloud is classified as fog.

Finally, after the day or night portion of the algorithm, a spatial filter on cirrus and overlap pixels is applied, in which the minimum of $T_{11}$ and the mean of $\varepsilon_{3.8}$ in a 7x7 pixels box around the pixel of interest are considered.

s1: Spatial test to re-set cirrus to liquid

If a pixel is classified as cirrus with a low quality, and either the pixels in the box have MIN($T_{11}$) > 295 – 12(1-$\theta$) or MEAN($\varepsilon_{3.8}$) < 1.2, then the pixel is re-set to supercooled (if $T_{11} \leq 273.16$ K) or water (if $T_{11} > 273.16$ K).

s2: Spatial test to re-set overlap to liquid

If a pixel is classified as overlap, $\theta_0 > 90^o$, and the pixels in the box have MIN($T_{11}$) > 273 – 12(1-$\theta$), then the pixel is re-set to supercooled (if $T_{11} \leq 273.16$ K) or water (if $T_{11} > 273.16$ K).

The next step in the algorithm is a consistency check with the cloud-top temperature. Very cold clouds are not allowed to be liquid, and warm clouds are not allowed to be ice. Concretely, if the extended cloud phase is fog, water or supercooled and $T_c \leq 231$ K, it is re-set to cirrus or opaque (if cloud optical thickness has been retrieved and is larger than 3). If the extended cloud phase is opaque, cirrus or overlap, and $T_c \geq 265$ K, it is re-set to liquid.

Finally, the extended phase is reduced to a binary cloud-top phase product, by setting the categories fog, water and supercooled to liquid and the categories opaque ice, cirrus and overlap to ice. This phase enters the optical properties retrieval. As explained in the next section, it is possible that the optical properties retrieval is inconsistent with the assigned phase. In that case, the phase is switched (from liquid to ice or vice versa) and the extended phase is switched accordingly. With that last step, which is obviously only applied during daytime, the cloud-top phase product is ready.

### 4.3.2. Cloud optical properties

For the cloud optical property retrieval, the observed VIS and NIR reflectances are compared with the simulated reflectances in the LUT. In case the 3.8-μm channel is used as NIR channel, the observed radiance is expressed as a reflectance:

$$R_{3.8} = \frac{\pi L_{3.8}}{\mu_0 F_{0,3.8}}, \qquad (13)$$

which is then compared with the sum of simulated solar reflectance (from the DAK LUT) and thermal emission cast as a reflectance (from Eq. (6)). The cloud optical thickness and particle size are retrieved in an iterative manner for cloudy pixels during daytime ($\theta_0 < 84^o$). During the iteration the retrieval of τ at the 0.6-μm channel is used to update the retrieval of $r_e$ at the 1.6/3.8-μm channel, and vice versa. This iteration process continues until the retrieved cloud optical properties converge to stable values. The interpolation between cloud optical properties in the LUTs is done with polynomial interpolation in τ and linear interpolation in $\log(r_e)$. As stated in Section 4.2, the retrieved particle size values are unreliable for optically thin clouds. Therefore for thin clouds the retrieved effective radius is adjusted towards an assumed climatologically averaged effective radius of 8 μm and 26 μm for water and ice clouds, respectively, values that are close to the ones used by Rossow and Schiffer (1999). The adjustment is performed for clouds with $\tau < 8$ using a smooth weighting function that gives an increasing weight to the climatologically averaged effective radius with decreasing cloud optical thickness. At 3.8 μm the adjustment of $r_e$ is applied for $\tau < 5$ because there is more information on $r_e$ for thin clouds in this channel due to the stronger absorption,

## 4.4. ERROR BUDGET ESTIMATES

The retrieval of cloud optical thickness and effective radius from 2-channel backscattered solar radiation is a simple but heavily underconstrained problem. As a result, many uncertainties are associated to this retrieval problem (see Stephens and Kummerow (2007) for a review). Here we attempt to describe some of the most important error sources. In Section 5, further sources of uncertainty related to violation of basic retrieval assumptions are discussed.

*Errors in radiative transfer*

To assess the potential error caused by uncertainties in radiative transfer modeling, Roebeling et al. (2005) compared four well-known RTMs that use different methods to solve the equation of radiative transfer. All these models are suited for simulating short-wave and narrow-band radiances in a cloudy atmosphere. However, the codes have originally been developed and optimized for different applications. The following methods for solving radiative transfer were compared:

- Monte Carlo method

The Monte Carlo model (Macke et al. 1999) is a forward scheme with a local estimate procedure for radiance calculations. It is a straightforward model that can be extended from one-dimensional to two- or three-dimensional calculations (Davis et al. 1985). Monte Carlo treats multiple scattering as a stochastic process. The phase function governs the probability of scattering in a specific direction. Photons are emitted by a source (e.g. the sun or a lidar device) and undergo scattering and absorption events inside a predefined three-dimensional cloudy atmosphere until: (i) the intensity of the photons falls below a certain threshold (due to absorption), (ii) the photons escape from the system. After each scattering event, the intensity of the photons that contribute to predefined sensor viewing angles is calculated (local estimate procedure).

- Doubling Adding method

This is the method used in the DAK model introduced in Section 4.2. DAK first calculates the reflection and transmission of an optically thin layer, in which no more than two scattering events may occur. Thanks to this restriction the radiative transfer equation can be solved analytically. Next, the reflection and transmission of two identical layers on top of each other can be obtained by computing successive reflections back and forth between the layers. This doubling procedure is continued until the actual optical thickness of the cloud is reached. The cloud is embedded in a multilayer Rayleigh scattering atmosphere. The DAK model includes polarization.

- Discrete Ordinates method

In the MODerate spectral resolution atmospheric TRANsmittance and radiance code (MODTRAN), the multiple scattering calculations are based on the Discrete Ordinate (DISORT) method (Stamnes et al. 1988). The radiative transfer equation is solved for $N$ discrete zenith angles to obtain $N$ equations for $N$ unknowns. These unknowns may be solved numerically. The MODTRAN single scattering radiances are computed separately from DISORT with inclusion of spherical geometry effects; the plane-parallel DISORT single scattering contributions are subtracted from the DISORT radiances for generation of the total radiance values. For the comparisons a beta version, MODTRAN4v2r0, was used, in which user-defined phase functions for cloud particles could be specified.

- Spherical Harmonics Discrete Ordinates method

The Spherical Harmonics Discrete Ordinate Method SHDOM (Evans 1998) has been developed for modelling radiative transfer in inhomogeneous three-dimensional media. SHDOM uses an iterative procedure to compute the source function of the radiative transfer equation on a grid of points in space. The angular part of the source function is represented by a spherical harmonics expansion mainly because the source function is computed more efficiently in this way than in DISORT. A discrete ordinate representation is used in the solution process. The number of iterations increases with increasing single scattering albedo and optical thickness.

The intercomparison study demonstrated that SHDOM and DAK are suitable models for the calculations of narrow-band cloud reflectances. For a clear atmosphere all models showed small absolute differences relative to the reference model (Monte Carlo), while for a cloudy atmosphere considerably larger absolute differences were observed. The causes for the latter differences are due to numerical noise or differences in the multiple scattering calculations. The implementation of a user-defined phase function in MODTRAN4v2r0 (beta release) was a large improvement, it was still the least accurate model for the simulation of cloud reflectances in this study. On average MODTRAN simulations deviated less than 3% from the reference model, but for individual viewing angles in the principal plane the deviations can increase to about 30%. It was suggested that the differences in MODTRAN reflectances cannot be fully explained by the

method for multiple scattering calculations (DISORT). Part of the observed differences may be explained by different or incorrect model parameterizations. However, MODTRAN has been further improved since the study by Roebeling et al. (2005). The DAK and SHDOM calculations were similar to Monte Carlo, with mean differences smaller than 3%. However, for individual cases the differences were occasionally much larger. A noticeable finding was that the Monte Carlo has a 3% bias as compared to SHDOM and DAK. This bias may be explained by differences in the treatment of the forward peak of the scattering phase function. Especially for large particles with a strong forward peak this may cause significant differences in simulated reflectances. Beside these differences, Monte Carlo showed small non-systematic oscillations relative to SHDOM and DAK. These oscillations were largest for optically thick clouds ($\tau$ = 64), for moderate particle sizes ($r_e$ = 10 μm) and for large viewing zenith angles (75°). For these cases the number of multiple scattering events is large (up to 200) and the forward peak is strong, such that small differences in single scattering parameters can easily accumulate to large errors in the reflectances (±2%). Finally, the used version of SHDOM became unstable at certain optical thicknesses and effective radii. Comprehensive analysis showed that these instabilities occur at 0.63 and 1.61 μm wavelengths and that the problem disappeared again by choosing another optical thickness or effective radius.

### *Instrument errors*

The solar channels of the satellite instruments covered in this ATBD are not calibrated on-board. For AVHRR the pre-flight calibration coefficients for the solar channels have been shown to be sometimes off by tens of percents (Heidinger et al. 2002). Recalibration using ground targets and other satellite instruments, such as MODIS, is thus crucial, and enhances the accuracy to typically 2-3% (Heidinger et al. 2010). The thermal channels are normally in a better shape because they are calibrated on board using blackbodies.

Errors in the observed reflectance translate non-linearly into errors in retrieved cloud properties, since the relationship between reflectance and cloud properties is non-linear. The CPP algorithm includes an error estimate for this retrieval error. We start from the functional relationship $R_{V,N}$ = f($\tau$,$r_e$), where $R_{V,N}$ is the reflectance in the VIS or NIR channel. Derivation of this relation leads to:

$$\Delta R_{V,N} = \left.\frac{\partial R_{V,N}}{\partial \tau}\right|_{r_e} \Delta\tau + \left.\frac{\partial R_{V,N}}{\partial r_e}\right|_{\tau} \Delta r_e, . \qquad (14)$$

where Δ denotes an error. The partial derivatives with respect to τ ($r_e$) are at constant $r_e$ (τ), respectively. Eq. (14) can be inverted to:

$$\Delta\tau = \frac{1}{F}\left( \left.\frac{\partial R_N}{\partial r_e}\right|_{\tau} \Delta R_V - \left.\frac{\partial R_V}{\partial r_e}\right|_{\tau} \Delta R_N \right); \qquad (15)$$

$$\Delta r_e = \frac{1}{F}\left( -\left.\frac{\partial R_N}{\partial \tau}\right|_{r_e} \Delta R_V + \left.\frac{\partial R_V}{\partial \tau}\right|_{r_e} \Delta R_N \right), . \qquad (16)$$

with

$$. \; F = \frac{\partial R_V}{\partial \tau}\bigg|_{r_e} \frac{\partial R_N}{\partial r_e}\bigg|_{\tau} - \frac{\partial R_V}{\partial r_e}\bigg|_{\tau} \frac{\partial R_N}{\partial \tau}\bigg|_{r_e} . \qquad (17)$$

The retrieval error in LWP follows directly from the errors in τ and $r_e$. These relations are applied in CPP with a 3% relative error in the VIS and NIR reflectance. The resulting error estimates relate to the propagation of reflectance errors into errors in retrieved cloud properties, and do not cover error sources discussed further on in this document.

Figure 4 shows the estimated retrieval errors for typical conditions, and their dependence on the cloud properties. Two important features are illustrated by this figure. First, the cloud optical thickness retrieval becomes highly uncertain for thick clouds as a result of the asymptotic relation between visible reflectance $R$ and cloud optical thickness $\tau$. The derivative $d\tau/dR$ increases with increasing $\tau$, and for large values of $\tau$ a marginal change in visible reflectance causes a large increase in the retrieved cloud optical thickness. Second, the error in effective radius is generally between 2 and 3 μm, but becomes much larger for thin clouds. For this reason the retrieval of $r_e$ for thin clouds is weighed towards a climatological value, as was discussed in Section 4.3. Figure 4 shows that errors get larger at high solar zenith angles, but not dramatically. Errors may increase more for particular parts of the phase function, e.g. the backward scattering peak or the rainbow.

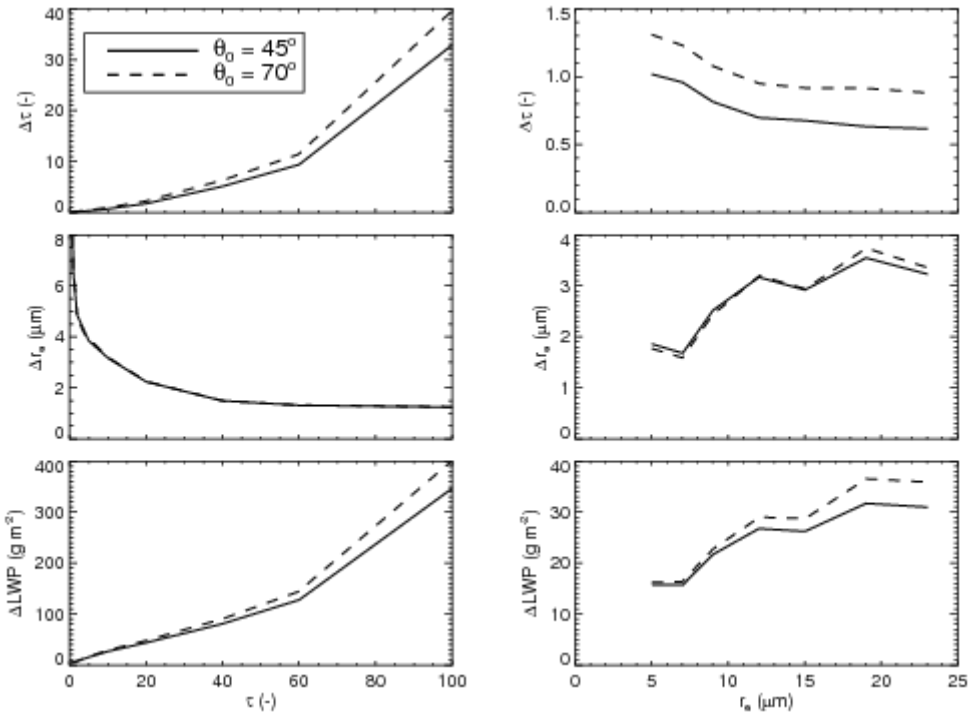


*Figure 4 CPP retrieval errors as calculated using Eq. (14)-(17). The errors in τ (top),* $r_e$ *(middle), and LWP (bottom) are shown as a function of τ (left, with* $r_e$ *= 12 μm kept constant) and* $r_e$ *(right, with τ = 10 kept constant). The calculations were done for* $\theta_0$ *= 45° and* $\theta_0$ *= 70°,* θ *= 30° and* φ *= 90°, and are based on the 0.6-/1.6-μm channel combination.*

### *Errors in ancillary data*

A significant source of retrieval error is caused by uncertainties in surface reflectance $\alpha_s$. This is illustrated in Figure 5, which displays the impact on retrieved LWP of a – realistic – 25% (relative) uncertainty in $\alpha_s$. Deviations of $\alpha_s$ in the non-absorbing channel (left panels) mainly

affect the retrieved cloud optical thickness. The impact is relatively largest for thin clouds because the TOA outgoing radiation over these clouds contains a considerable contribution from the surface. Deviations of $\alpha_s$ in the absorbing channel (right panels) mainly affect the retrieved effective radius. This impact is also largest for thin clouds, but due to the weighing with a climatological effective radius it is suppressed for the thinnest clouds. Hence, a maximum sensitivity is observed for an optical thickness around 5. In all cases LWP is more sensitive to uncertainties in $\alpha_s$ over the brighter land surfaces than over the darker ocean. Over ice- and snow-covered surfaces, with a typical 0.6-μm surface albedo of 0.8, the retrieval becomes extremely sensitive, with LWP deviations of over 100% (not shown in Figure 5).

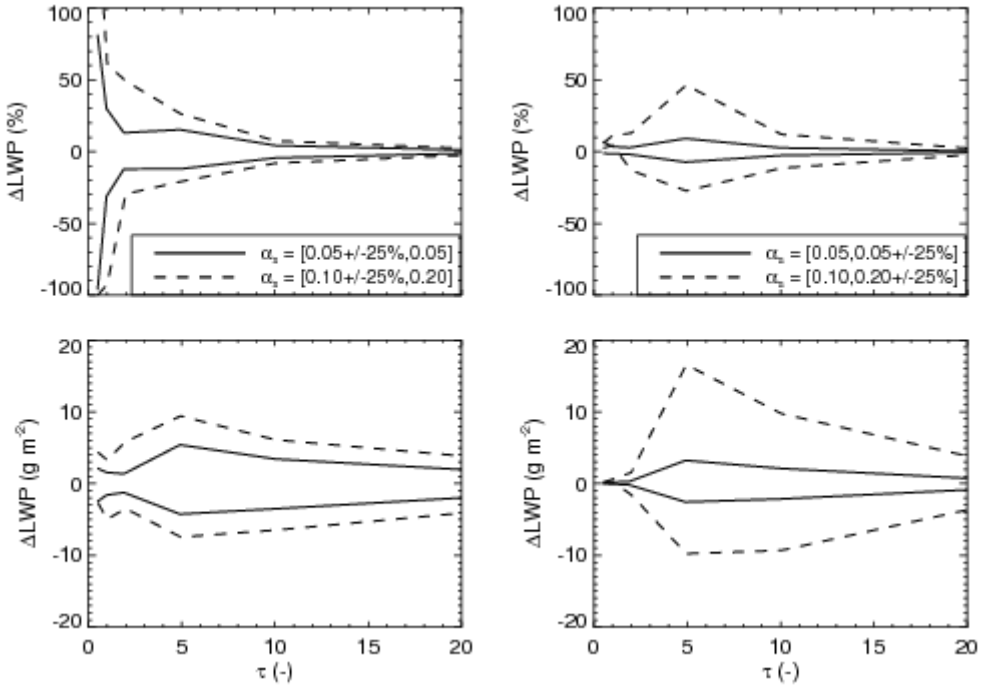


*Figure 5 Sensitivity of retrieved LWP to uncertainties in surface reflectance. The curves show the relative (top panels) and absolute (bottom panels) deviation of LWP from the truth following from retrievals with a 25% increased or decreased surface reflectance in the 0.6-μm (left panels) and 1.6-μm (right panels) as a function of the true optical thickness. Two types of surfaces are distinguished: ocean with $\alpha_s$ = 0.05 at 0.6 and 1.6 μm (solid lines) and land with $\alpha_s$ = 0.1 at 0.6 and $\alpha_s$ = 0.2 at 1.6 μm (dashed lines). The calculations were done for $\theta_0$ = 45°, $\theta$ = 30° and $\varphi$ = 90°.*

Another source of error is the ancillary data needed for the atmospheric correction. The largest impact is expected from uncertainties in the water vapour path and to a lesser extent the total ozone column. Errors in geolocation, solar angles and satellite angles can be assumed to be small, and hence their impact on cloud property retrievals is limited. Finally, the cloud mask, which is external input to the CPP algorithm (and thus considered here as ancillary data), is of importance. The cloud mask determines for which satellite pixels, a retrieval is performed. It does not influence the retrieval itself, i.e. the level-2 products, but is does have impact on aggregated level-3 products. Typically, a more selective cloud mask (i.e. assigning less pixels cloudy) leads to a larger aggregated cloud optical thickness for the cloudy portion of the sky.

## 4.5. PRACTICAL APPLICATION

This section provides details on the satellite instruments (AVHRR, VIIRS, and MODIS) and other input data used by the CPP algorithm.

### 4.5.1. Satellite instruments

NOAA has launched a series of polar orbiting satellites that carry the AVHRR instrument. Recently, EUMETSAT also launched an AVHRR instrument on the METOP polar orbiting satellite. The AVHRR passive imager operates six channels at wavelengths between 0.5 and 12.0 μm. Table 9 summarizes the AVHRR channels used by CPP. Due to fundamental constraints, the near-infrared 1.6 μm and 3.8 μm channels are time-shared. On NOAA-16 (during the first two years of its life), NOAA-17, and METOP the 1.6-μm channel has been operated during the daylight part of the orbit, while the 3.8-μm channel was operated during night. All other NOAA satellites have only transmitted data from the 3.8-μm channel. The spatial resolution of all channels at nadir is around 1x1 $km^2$, but this is degraded to 5x4 $km^2$ for GAC-AVHRR.

*Table 9: AVHRR channels used by CPP*

| *Channel* | *Central wavelength (μm)* | *Nominal spectral band (μm)* |
|---|---|---|
| ***1*** | 0.63 | 0.58 - 0.68 |
| ***3a*** [a)] | 1.61 | 1.58 - 1.64 |
| ***3b*** [a)] | 3.74 | 3.55 - 3.93 |
| ***4*** | 10.8 | 10.30 - 11.30 |
| ***5*** | 12.0 | 11.50 - 12.50 |

[a)] Only one NIR channel at the same time can be transmitted to the ground.

NOAA has also launched the polar satellite NPP, which will be followed by a series of JPSS satellites. All of them carry the sensor VIIRS. Table 10 summarizes the VIIRS channels used by CPP. The spatial resolution of these channels is 750 x 750 $m^2$ at nadir. CPP can be run with VIIRS data either M10 or M12 as absorbing channel.

*Table 10: VIIRS channels used by CPP.*

| *Channel* | *Central wavelength (μm)* | *Nominal spectral band (μm)* |
|---|---|---|
| ***M5*** | 0.672 | 0.662 - 0.682 |
| ***M10*** | 1.61 | 1.58 - 1.64 |
| ***M12*** | 3.70 | 3.61 - 3.79 |
| ***M15*** | 10.76 | 10.26 - 11.26 |
| ***M16*** | 12.01 | 11.54 - 12.49 |

CPP can also be run in high resolution, using a combination of VIIRS data from the I-band and M-band channels. Table 11 describes which channels are needed The spatial resolution for the I-band channels is 375 x 375 $m^2$ at nadir. The M-band channels are interpolated to that resolution, before using them in PPS.

*Table 11: VIIRS channels used by CPP, for running in high resolution.*

| *Channel* | *Central wavelength (μm)* | *Nominal spectral band (μm)* |
|---|---|---|
| ***I1*** | 0.64 | 0.60-0.68 |
| ***I3*** | 1.61 | 1.58-1.64 |
| ***I4*** | 3.74 | 3.55-3.93 |
| ***M15*** | 10.76 | 10.26 - 11.26 |
| ***M16*** | 12.01 | 11.54 - 12.49 |

The MODIS instrument on board the EOS-Terra and EOS-Aqua platforms has 36 channels. Table 12 summarizes the channels used by CPP. The spatial resolution of these channels varies from 250 x 250 $m^2$ to 1 x 1 $km^2$.

*Table 12: MODIS channels used by CPP.*

| *Channel* | *Central wavelength (μm)* | *Nominal spectral band (μm)* |
|---|---|---|
| ***1*** | 0.645 | 0.620 - 0.670 |
| ***6*** | 1.640 | 1.628 - 1.652 |
| ***20*** | 3.750 | 3.660 - 3.840 |
| ***31*** | 11.03 | 10.78 - 11.28 |
| ***32*** | 12.02 | 11.77 - 12.27 |

The MERSI-2 instrument will be launched on the FY-3D and FY-3E satellites. It has 25 channels at a spatial resolution varying between 250 x 250 $m^2$ and 1 x 1 $km^2$. Table 13 summarizes the channels used by CPP. MERSI-2 usage is TBD01.

*Table 13: MERSI-2 channels used by CPP. Exact channel specifications (spectral response functions) are not yet available.*

| *Channel* | *Central wavelength (μm)* | *Nominal spectral band (μm)* |
|---|---|---|
| ***7*** | 0.650 | 0.625 - 0.675 |
| ***18*** | 1.640 | 1.615 - 1.665 |
| ***20*** | 3.80 | 3.71 - 3.89 |
| ***24*** | 10.8 | 10.3 - 11.3 |
| ***25*** | 12.0 | 11.5 - 12.5 |

### 4.5.2. Input data

In this section, the required input data for the algorithms are described.

#### *4.5.2.1 Radiances*

Radiances from 0.6-μm, 1.6-μm, 3.8-μm, 11-μm, and 12-μm channels are the basic input.

#### 4.5.2.2 Solar and satellite angles

The solar zenith angle $\theta_0$, the satellite viewing zenith angle $\theta$, and the relative sun-satellite azimuth angle $\phi$ are required. These angles are calculated by the NWC-SAF software and provided as input to CPP.

#### 4.5.2.3 Cloud mask

A cloud mask is needed to decide for which pixels a cloud physical properties retrieval will be attempted. As default, the cloud mask (CMa) of the NWC-SAF is used for this purpose (see [RD.5]). The CPP retrievals are run for pixels classified as *cloud contaminated* or *cloud filled*.

An alternative input (configurable) is the Cloud Probability (CMa-prob) product instead. The CPP retrievals are run for pixels with a cloud probability of 50% or more. (Configurable via environment variable SM_CMAPROB_CLOUD_THRESHOLD.)

#### 4.5.2.4 Cloud top height and temperature

CPP uses the cloud top temperature and height, which are taken from the CTTH product from NWC-SAF ([RD.6]). It can also manage without the CTTH-product, or with only one of cloud top temperature or height available.

#### 4.5.2.5 Surface albedo

Over land this is prescribed from a 5-year mean MODIS 0.6- and 1.6-µm snow-free gap-filled white-sky surface albedo database with 16-day resolution (Moody et al., 2004, 2008). This database was chosen because: (i) it is a frequently used and well recognized dataset; (ii) it contains the spectral channels needed for CPP processing; (iii) it has global extension and (iv) it is gap-filled. Over ocean the surface albedo is assumed to be 0.05 at both 0.6 µm and 1.6 µm, and 0.02 at 3.8 µm.

#### 4.5.2.6 Surface emissivity

For the 3.8-µm retrieval, a climatology compiled from four years of the MODIS-based surface emissivity database by Seemann et al. (2008) is used over land, while over ocean the surface emissivity is set to 0.98. The motivation for chosing this dataset was similar as for the surface albedo dataset. Another advantage is that the surface albedo and surface emissivity datasets are consistently based on MODIS observations.

#### 4.5.2.7 Numerical Weather Prediction (NWP) model fields

The following NWP model fields are required:

- Surface temperature. This is needed only for the 3.8-µm retrieval.
- Water vapour path. For the atmospheric correction the water vapour path is needed. As a back-up it is possible to use a monthly-mean climatology based on ERA-Interim data.
- Snow depth and snow albedo. These are used for the cloud phase determination and to correct the MODIS snow-free albedo in case of snow on the ground. The snow

parameters are not mandatory input, in the sense that the algorithm will still run if they are missing, but obviously with lower quality in snow-affected areas.

The NWP fields are obtained from operational ECMWF data or ERA-Interim.

#### 4.5.2.8 Sea ice concentration

The concentration of sea ice is used for the cloud phase determination and to correct the albedo of sea for the presence of ice. It is obtained from the OSI-SAF. (Either operational products, or re-processed.) Like the snow parameters, this input is not mandatory.

#### 4.5.2.9 Ozone

A monthly mean total ozone column climatology at 1 x 1.5 degrees was generated from the Multi Sensor Reanalysis (MSR) dataset (Van der A et al., 2010). This is needed as input for the atmospheric correction. All ozone is assumed to reside above the clouds.

### 4.5.3. Description of Output

The output file contains seven datasets with products, three datasets with error estimates and three processing flags. Here, for each dataset in SAFNWC/PPS, the name, the data it contains and the units are listed. The physical data are implemented with scale factor, add offset and no-data-value, of which the values can be read in the file. All products except cpp_phase and cpp_phase_extended are available only in daylight conditions ($\theta_0 < 84^o$).

**cpp_phase**: Cloud-top thermodynamic phase, classes: liquid, ice

**cpp_phase_extended**: Cloud-top thermodynamic phase, extended to more classes. Classes: clear, fog, water, super-cooled, mixed, opaque_ice, cirrus, overlap

**cpp_lwp**: Cloud liquid water path, unit: kg/m$^2$

**cpp_iwp**: Cloud ice water path, unit: kg/m$^2$

**cpp_cwp**: Cloud water path, unit: kg/m$^2$

**cpp_cot**: Cloud optical thickness, dimensionless

**cpp_reff**: Cloud particle effective radius, unit: m (though typical values are in the µm-range)

**cpp_dcwp**: Error estimate for cloud water path, relates to cpp_cwp, but is also valid for cpp_lwp and cpp_iwp, unit: kg/m$^2$

**cpp_dcot**: Error estimate for cloud optical thickness, relates to cpp_cot, dimensionless

**cpp_dreff**: Error estimate for cloud particle effective radius, relates to cpp_reff, unit: m

**cpp_conditions**: flag for geophysical and processing conditions, bit flag, described below

**cpp_quality**: flag for quality indicators, bit flag, described below

**cpp_status_flag**: flag for processing conditions and status, bit flag, described below

The formulations of the flags cpp_conditions and cpp_quality are common with the other SAFNWC/PPS PGEs, though the content is updated for CPP (e.g., quality criteria are specific,

while land/sea is the same for all PGEs). The formulation of the cpp_status_flag is specific for the CPP product.

*Table 14 CPP conditions and processing flags*

| **Bit number** | **Flag: cpp_quality** | **Explanation** |
|---|---|---|
| 0 | Non-processed | Containing no data. Cloud-free pixel or pixel for which no product could be retrieved. |
| 1 | Spare | |
| 2 | Spare | |
| 3-5 | Quality | 0: N/A nodata<br>1: Good<br>2: Questionable (Set when there is snow or ice at the surface or when the cloud phase has been changed by the optical properties retrieval)<br>3: Bad (Set when the NIR reflectance is outside the range of the look-up-table)<br>4: Interpolated/Reclassified (Set when the pixel has been reset to clear by the optical properties retrieval) |
| **Bit number** | **Flag: cpp_status_flag** | **Explanation** |
| 0 | Cloud-free | Cloud-free |
| 1 | Bad optical conditions | When the optical conditions are too bad for retrieving cwp, cot and reff (too high solar zenith angle) |
| 2 | Snow/ice | There is suspected snow or ice at the surface |
| 3 | 1.6 micron used | The 1.6 μm channel has been used for the retrieval. |
| 4 | 3.8 micron used | The 3.8 μm channel has been used for the retrieval. |
| **Bit number** | **Flag: cpp_conditions** | **Explanation** |
| 0 | Outside swath | Pixel is outside swath (can occur after remapping to region) |
| 1-2 | Illumination | day/night/twilight |
| 3 | Sunglint | possibly sun glint |
| 4-5 | Land Sea | land/sea/coast |
| 6 | High Terrain | high terrain |
| 7 | Rough Terrain | rough terrain |
| 8-9 | Satellite input data | Satellite data is available/missing |
| 10-11 | NWP input data | NWP data (surface temperature and total water vapour) is available/missing |
| 12-13 | Product input data | Cloud mask data is available/missing |
| 14-15 | Auxiliary input data | Auxiliary data is available/missing |

# 5. ASSUMPTIONS AND LIMITATIONS

In this section some of the assumptions and limitations associated with the retrieval algorithms are listed. There are also general limitations related to the characteristics of the satellite instruments. For example, GAC-AVHRR has a nominal resolution of 5x4 $km^2$, compared to 1x1 $km^2$ for LAC-AVHRR. A coarser resolution gives rise to systematic biases in the derived cloud physical properties, as outlined below. Also, polar orbiters have only two overpasses per day in the tropics (of which one during nighttime) and up to ≈8 near the poles. Thus, coverage of the diurnal cycle of cloud properties is limited.

Specific limitations for the cloud physical products include:

- The derivation of cloud optical properties from reflected solar radiation is dependent on the availability of daylight. This means that no retrievals of cloud optical thickness, effective radius and liquid/ice water path can be done during night time. However, cloud phase can be (and is) retrieved during night time, albeit with less spectral information being available and consequently lower overall product quality.

- Sunglint can affect the cloud property retrievals considerably, in particular for broken cloudy scenes over ocean. Therefore, possibly sunglint-affected pixels (defined by a scattering angle differing more than 25 degrees from the direct glint angle) over ocean are flagged.

- Cloud retrievals are performed assuming that clouds are plane parallel. This is true only in a minority of cases, which implies that retrieval errors become larger as clouds deviate from being plane parallel. Especially convective clouds can be problematic, as they frequently have illuminated and shadowed sides (see, e.g., Marshak et al. 2006). Broken cloud fields can also cause problems for retrieving cloud properties, since a passive satellite sensor measures an averaged radiance of the cloudy and cloud-free part of a pixel. The error made in these cases is among others dependent on the contrast between clouds and underlying surface, the true properties of the cloud, and the cloud fraction within the sampling resolution of the instrument (Oreopoulos and Davies 1998; Coakley et al. 2005; Wolters et al. 2010).

- The retrieval is highly problematic over very bright surfaces, particularly ice and snow, as the visible reflectance from clouds is similar to that from the surface.

- Unlike active satellite instruments, which can derive cloud profile information, retrievals from passive satellite instruments are limited by the fact that the obtained signal emanates from the integrated profile. Since near-infrared radiation is only penetrating into the cloud to a certain depth (due to absorption by cloud particles), the retrieved cloud phase and effective radius are representative for the upper part of the cloud (Platnick 2001). The penetration depth depends on the amount of absorption by cloud particles, which is increasing with wavelength. This means that the retrieved CPH and $r_e$ depend on which NIR spectral channel is used (in our case 1.6 or 3.8 μm). See, for example, Rosenfeld et al. (2004) for a discussion on pros and cons of the use of different NIR channels. Seethala and Horvath (2010) and Zhang and Platnick (2011) noted that the 3.8 μm $r_e$ can be significantly smaller than the 1.6 or 2.2 μm $r_e$ in non-raining Sc clouds, for which one would expect, in contrast, a steady increase in $r_e$ from 1.6 through 2.2 to 3.8 micron. They suggested that drizzle and/or 3D inhomogeneity effects might be the cause. Zhang et al. (2012) further investigated the effects of drizzle and cloud horizontal inhomogeneity on MODIS $r_e$ retrievals using LES models and synthetic retrievals and found that drizzle does not have a strong impact but inhomogeneity, the plane-parallel bias, does.

- In the derivation of equation *3* for LWP and IWP it is assumed that the cloud particle effective radius is representative for the total column . In reality this assumption is not assured. For example, liquid water clouds often obey adiabatic theory leading to a different relation form of Eq. (3), in which the factor 2/3 is replaced by 5/9, with $r_e$ defined as the effective radius at the cloud top. However, radiation at 1.6 μm penetrates a significant depth into the cloud, so that the derived $r_e$ is representative of a larger vertical extent as compared to retrievals using channels at 2.1 or 3.8 μm. Seethala (2011) showed that for marine stratocumulus clouds, LWP derived using the SEVIRI 1.6 μm channel and a factor 2/3 in Eq. (3) is comparable to LWP derived using the MODIS 2.1 μm channel and a factor 5/9 in Eq. (3). This suggests that automatic adiabatic correction is applied by using the 1.6 μm channel. Deviations from vertical homogeneity are also common for ice clouds. Thick ice clouds often have small ice crystals at the top, which are not representative of the full vertical extent. As a consequence, IWP can be underestimated in these cases. Results are even more questionable for multi layer cloud systems. Here the derived effective radius (uppermost cloud) may be totally unrelated to any cloud below. So the relation between $r_e$ and LWP/IWP is not applicable here. However, multi layer clouds are known to be the most difficult systems to handle and no satisfying solution is known yet.

- Aerosols are not considered in the CPP retrieval. This assumption is usually justified because aerosols reside below or within the cloud and their optical thickness is small compared to that of the cloud. However, if the aerosols reside above the cloud and if they are sufficiently absorbing, they can significantly lower the visible reflectance. The effect on the retrievals depends on the channel combination used and on the aerosol properties (Haywood et al. 2004). The impact is strongest for the 1.6-μm channel, with a possible understimation of $r_e$ by several microns. For the 3.8-μm channel, the impact is smaller and can be an overestimation of $r_e$. Cloud optical thickness generally has a low bias. Although the annual mean effect of absorbing aerosols is relatively small, their instantaneous effect on LWP can be as high as a 40 g $m^{-2}$ low bias, mostly caused by a reduction in optical thickness. Wilcox et al. (2009) and Seethala and Horvath (2010) both have given estimates of absorbing aerosol effects on MODIS LWP by comparing it with passive microwave retrievals and quantifying the aerosol load with the help of OMI aerosol index. Seethala (2011) obtained similar estimates for SEVIRI LWP by comparison to TMI microwave retrievals.

- Precipitation may have an effect on cloud property retrievals in case the radiation penetrates sufficiently deep into the cloud to be affected by the (large) precipitating droplets. Retrievals with the 1.6-μm channel are expected to be most sensitive to this, but synthetic studies (e.g., Zinner et al. 2010; Zhang et al. 2012) have not indicated significant impact on the effective radius retrieval.

- Many assumptions are made for the calculation of LUTs with DAK. These include: the absence of aerosols, the location of the cloud between 1 and 2 km height, the specific habits and resulting phase functions of ice crystals, and the type and width of water droplet effective radius distributions. The necessity of these assumptions is an illustration of the heavily underconstrained nature of the cloud physical properties retrieval principle.

- While the cloud phase product has been validated for instantaneous values against Calipso data over both land and sea, the LWP product has only been properly validated for instantaneous values over sea using AMSR-E data. Though there has been made a comparison with MODIS liquid water path, split in land and sea, and it show about as good performance over land as over sea. See Validation report for validation results, and discussion of land validation [RD.4].

# ANNEX A. List of TBC, TBD, Open Points and Comments

| TBD/TBC | Section | Resp. | Comment |
|---|---|---|---|
| TBD01 | 4.5.1 | SMHI | MERSI-2 capabilities will be provided later as a patch to v2018, if and when, necessary info and data are available. |

# ANNEX B. Thresholds used in the cloud phase algorithm

The cloud phase algorithm described in Section 4.3.1 contains a number of thresholds, the settings of which are detailed here.

NIR_PHASE_THRES

| Channel | Water or snow/ice | Other |
|---|---|---|
| 1.6 μm | 0.17 | 0.32 |
| 3.8 μm | 0.06 | 0.06 |

NIR_CIRRUS_THRES

| Channel | Water or snow/ice | Desert | Other |
|---|---|---|---|
| 1.6 μm | 0.20 | 0.55 | 0.33 |
| 3.8 μm | 0.12 | 0.40 | 0.12 |

NIR_OVER_THRES

| Channel | Snow/ice | Other |
|---|---|---|
| 1.6 μm | 0.17 | 0.0 |
| 3.8 μm | 0.06 | 0.0 |

BTD1112_DOVERLAP_THRES

- $0.35 \leq R_{0.6} \leq 0.60$: MAX($a_0 + a_1 R_{0.6} + a_2 (R_{0.6})^2 + \ldots + a_4 (R_{0.6})^4$, MIN_BTD1112_DOVERLAP) – 0.1
- $0.60 < R_{0.6} < 0.90$: MIN_BTD1112_DOVERLAP - 0.1

If $R_{0.6} < 0.35$ or $R_{0.6} \geq 0.90$, the threshold is not applied. In addition, for latitudes poleward of 65 degrees, and if $R_{3.8} > 0.2$, the threshold is not applied.

The coefficients $a_0$ to $a_4$ and MIN_BTD1112_DOVERLAP are functions of $\theta$ and $\theta_0$ (in 10-degree bins)

$a_0$

| $\theta_0$ \ $\theta$ | 0-10 | 10-20 | 20-30 | 30-40 | 40-50 | 50-60 | 60-70 |
|---|---|---|---|---|---|---|---|
| 0-10 | 2.94 | 3.14 | 3.15 | 3.03 | 3.27 | 3.77 | 3.77 |
| 10-20 | 2.94 | 3.14 | 3.15 | 3.03 | 3.27 | 3.77 | 3.77 |
| 20-30 | 2.76 | 3.04 | 3.14 | 3.20 | 3.23 | 3.25 | 3.25 |
| 30-40 | 2.95 | 2.75 | 3.03 | 3.15 | 3.34 | 3.48 | 3.48 |
| 40-50 | 2.62 | 2.71 | 2.65 | 2.80 | 2.80 | 2.97 | 2.97 |
| 50-60 | 2.26 | 2.59 | 2.33 | 2.43 | 2.62 | 3.01 | 3.01 |
| 60-70 | 1.94 | 1.29 | 1.65 | 1.65 | 1.88 | 0.649 | 0.649 |
| 70-80 | -2.33 | -1.83 | 0.417 | -2.67 | -0.72 | 0.234 | 0.234 |

$a_1$

| $\theta_0$ \ $\theta$ | 0-10 | 10-20 | 20-30 | 30-40 | 40-50 | 50-60 | 60-70 |
|---|---|---|---|---|---|---|---|
| 0-10 | .936 | -3.25 | -2.60 | 1.71 | -.743 | -8.27 | -8.27 |
| 10-20 | .936 | -3.25 | -2.60 | 1.71 | -.743 | -8.27 | -8.27 |
| 20-30 | 4.48 | -1.20 | -2.31 | 1.98 | .148 | 2.65 | 2.65 |
| 30-40 | .365 | 4.94 | -.240 | 1.20 | -2.60 | -2.09 | -2.09 |
| 40-50 | 6.62 | 4.96 | 6.72 | 5.76 | 8.27 | 9.71 | 9.71 |
| 50-60 | 12.1 | 6.67 | 11.2 | 10.5 | 9.62 | 7.24 | 7.24 |
| 60-70 | 16.7 | 24.5 | 19.9 | 19.9 | 18.1 | 33.7 | 33.7 |
| 70-80 | 69.2 | 62.6 | 35.3 | 65.7 | 45.8 | 35.6 | 35.6 |

$a_2$

| $\theta_0$ \ $\theta$ | 0-10 | 10-20 | 20-30 | 30-40 | 40-50 | 50-60 | 60-70 |
|---|---|---|---|---|---|---|---|
| 0-10 | -41,2 | -24.1 | -27.7 | -45.7 | -36.0 | -8.56 | -8.56 |
| 10-20 | -41,2 | -24.1 | -27.7 | -45.7 | -36.0 | -8.56 | -8.56 |
| 20-30 | -54.7 | -32.0 | -27.7 | -29.6 | -38.0 | -52.9 | -52.9 |
| 30-40 | -37.6 | -55.1 | -34.1 | -30.1 | -24.0 | 30.2 | 30.2 |
| 40-50 | -60.8 | -53.0 | -57.7 | -53.8 | -64.1 | -76.7 | -76.7 |
| 50-60 | -81.4 | -59.6 | -72.9 | -65.9 | -62.1 | -48.8 | -48.8 |
| 60-70 | -102 | -127 | -106 | -100 | -93.7 | -138 | -138 |
| 70-80 | -309 | -280 | --169 | -256 | -186 | -123 | -123 |

$a_3$

| $\theta_0$ \ $\theta$ | 0-10 | 10-20 | 20-30 | 30-40 | 40-50 | 50-60 | 60-70 |
|---|---|---|---|---|---|---|---|
| 0-10 | -50.9 | -38.3 | -42.0 | -55.2 | -48.0 | -31.6 | -31.6 |
| 10-20 | -50.9 | -38.3 | -42.0 | -55.2 | -48.0 | -31.6 | -31.6 |
| 20-30 | -60.2 | -43.6 | -40.1 | -41.4 | -46.7 | -63.6 | -63.6 |
| 30-40 | -46.7 | -58.1 | -42.0 | -37.9 | -32.5 | -41.1 | -41.1 |
| 40-50 | -62.5 | -54.9 | -54.2 | -49.9 | -56.3 | -71.3 | -71.3 |
| 50-60 | -77.2 | -60.2 | -62.8 | -51.3 | -47.0 | -32.2 | -32.2 |
| 60-70 | -100 | -112 | -89.6 | -76.5 | -70.4 | -84.0 | -84.0 |
| 70-80 | -285 | -252 | -149 | -182 | -128 | -52.1 | -52.1 |

$a_4$

| $\theta_0$ \ $\theta$ | 0-10 | 10-20 | 20-30 | 30-40 | 40-50 | 50-60 | 60-70 |
|---|---|---|---|---|---|---|---|
| 0-10 | 85.8 | 60.5 | 66.9 | 93.5 | 79.1 | 42.4 | 42.4 |
| 10-20 | 85.8 | 60.5 | 66.9 | 93.5 | 79.1 | 42.4 | 42.4 |
| 20-30 | 105 | 71.5 | 65.0 | 67.8 | 79.2 | 107 | 107 |
| 30-40 | 78.8 | 103 | 71.6 | 64.7 | 54.6 | 68.2 | 68.2 |
| 40-50 | 111 | 97.9 | 101 | 93.7 | 108 | 133 | 133 |
| 50-60 | 141 | 108 | 120 | 103 | 96.3 | 70.1 | 70.1 |
| 60-70 | 178 | 208 | 170 | 153 | 143 | 187 | 187 |
| 70-80 | 508 | 455 | 275 | 369 | 266 | 140 | 140 |

MIN_BTD1112_DOVERLAP

| $\theta_0$ \ $\theta$ | 0-10 | 10-20 | 20-30 | 30-40 | 40-50 | 50-60 | 60-70 |
|---|---|---|---|---|---|---|---|
| 0-10 | 0.70 | 0.70 | 0.70 | 0.70 | 0.75 | 0.80 | 0.80 |
| 10-20 | 0.70 | 0.70 | 0.70 | 0.70 | 0.75 | 0.80 | 0.80 |
| 20-30 | 0.70 | 0.70 | 0.70 | 0.70 | 0.75 | 0.80 | 0.80 |
| 30-40 | 0.70 | 0.70 | 0.70 | 0.70 | 0.75 | 0.80 | 0.80 |
| 40-50 | 0.70 | 0.70 | 0.70 | 0.70 | 0.75 | 0.80 | 0.80 |
| 50-60 | 0.70 | 0.70 | 0.70 | 0.70 | 0.75 | 0.90 | 0.90 |
| 60-70 | 0.75 | 0.75 | 0.75 | 0.80 | 0.80 | 0.90 | 0.90 |
| 70-80 | 0.75 | 0.75 | 0.75 | 0.80 | 0.80 | 0.90 | 0.90 |

BTD1112_CIRRUS_THRES = MAX( 1.0, MIN( $b_0 + b_1T_{11} + b_4(T_{11})^2 + ... + b_4(T_{11})^4$, 4.0 ),

The coefficients $b_0$ to $b_4$ are the following functions of $\theta$ (in 10-degree bins):

| θ / coeff | 0-10 | 10-20 | 20-30 | 30-40 | 40-50 | 50-60 | 60-70 |
|---|---|---|---|---|---|---|---|
| $b_0$ | -3.21578e3 | -2.94035e3 | -3.21256e3 | -3.47061e3 | -3.50486e3 | -5.08847e3 | -5.09507e3 |
| $b_1$ | 4.88463e1 | 4.47332e1 | 4.86994e1 | 5.27678e1 | 5.32849e1 | 7.75359e1 | 7.80031e1 |
| $b_2$ | -2.76528e-1 | -2.53526e-1 | -2.75139e-1 | -2.99072e-1 | -3.01970e-1 | -4.40956e-1 | -4.45700e-1 |
| $b_3$ | 6.90693e-4 | 6.33594e-4 | 6.85787e-4 | 7.48048e-4 | 7.55160e-4 | 1.10843e-3 | 1.12561e-3 |
| $b_4$ | -6.41179e-7 | -5.88096e-7 | -6.35206e-7 | -6.95628e-7 | -7.02035e-7 | -1.03800e-6 | -1.05900e-6 |

EMS38_PHASE_THRES

$T_{11} \leq 245$: 0.9
$T_{11} > 245$: 1.12

BTD1112_NOVERLAP_THRES_H/_L and EMS38_NOVERLAP_THRES_H/_L

| | -30 < latitude < 30 | \| latitude \| > 30 |
|---|---|---|
| BTD1112_NOVERLAP_THRES_H | 2.5 | 2.0 |
| BTD1112_NOVERLAP_THRES_L | 0.78 | 0.58 |
| EMS38_NOVERLAP_THRES_H | 5.0 | 2.0 (over water: 2.5) |
| EMS38_NOVERLAP_THRES_L | 1.1 | 1.0 (over water: 1.05) |

These thresholds are not applied if $T_{3.8}$-$T_{11} \leq 0$ or if the surface type is desert.